Leveraging Entropy and Crystal Structure Engineering in Prussian Blue Analogue Cathodes for Advancing Sodium-Ion Batteries

Yueyue He, Sören L. Dreyer, Tolga Akçay, Thomas Diemant, Reiner Mönig, Yuan Ma, Yushu Tang, Huifeng Wang, Jing Lin, Simon Schweidler, Maximilian Fichtner, Horst Hahn, Torsten Brezesinski,* Ben Breitung,* and Yanjiao Ma*

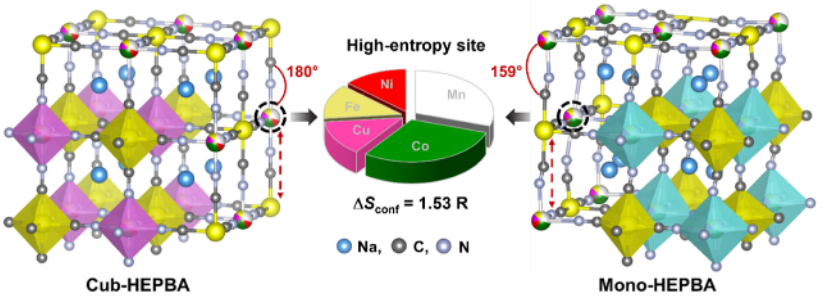

ABSTRACT: **The synergistic engineering of chemical complexity and crystal structures has been applied to Prussian blue analogue (PBA) cathodes in this work. More precisely, the high-entropy concept has been successfully introduced into two structure types of identical composition, namely, cubic and monoclinic. Through the utilization of a variety of complementary characterization techniques, a comprehensive investigation into the electrochemical behavior of the cubic and monoclinic PBAs has been conducted, providing nuanced insights. The implementation of the high-entropy concept exhibits crucial selectivity toward the intrinsic crystal structure. Specifically, while the overall cycling stability of both cathode systems is significantly improved, the synergistic interplay of crystal structure engineering and entropy proves particularly significant. After optimization, the cubic PBA demonstrates structural advantages, showcasing good reversibility, minimal capacity loss, high thermal stability, and unparalleled endurance even under harsh conditions (high specific current and temperature).**

KEYWORDS: *high-entropy materials, crystal structure, kinetics, phase transition, gas evolution, sodium-ion battery*

INTRODUCTION

The rapid evolution of society has been deeply rooted in the consumption of nonsustainable resources. This trajectory is forecasted to double, reaching 28 TW by 2050, equivalent to about 20 billion tons of oil annually.[1] In light of this trajectory, meeting the exponentially surging global energy demands necessitates a fundamental shift toward renewable energy sources and advanced energy-storage systems. This endeavor underscores the imperative to constantly unearth innovative materials to enable large-scale energy storage. As an emerging concept across scientific domains, including thermoelectrics,[2,3] catalysis,[4−6] environmental protection, and energy storage,[7−13] the high-entropy concept, which is based on the introduction of many different elements into a crystal structure, as well as on the exploitation of the elemental interactions that appear as a consequence, has sparked interest. High-entropy materials (HEMs), characterized by the incorporation of a minimum of five elements within a single-phase lattice and a resultant configurational entropy exceeding 1.5R (R being the gas constant), have triggered tremendous interest due to compositional flexibility and tailorable functional properties.[14]

The concept of HEMs is rooted in the endeavor to maximize the configurational entropy, thereby stabilizing complex atomic

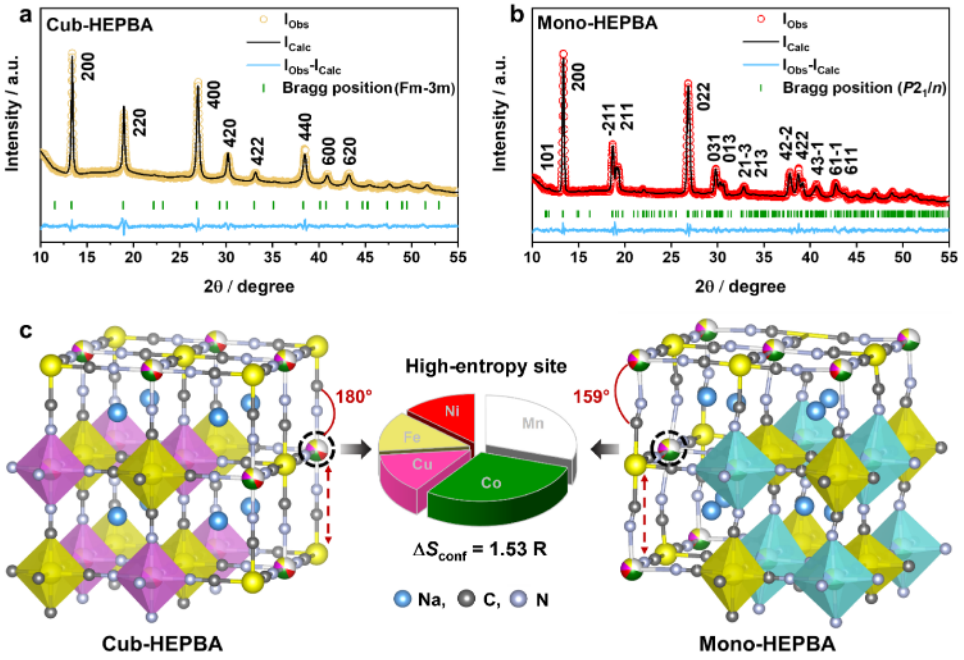

Figure 1. (a, b) Rietveld refinement analyses of XRD data collected from Cub- and Mono-HEPBA and (c) corresponding schematic illustrations of the crystal structure.

arrangements in nearly equimolar ratios. This leads to manifold interactions between the elements, commonly referred to as "cocktail effect". HEMs not only offer great chemical, but also sometimes the possibility to stabilize certain elemental mixtures that would not be miscible without high configurational entropy.[2] Notably, the landscape of innovative materials has witnessed a profound expansion of HEMs. This evolution, originating from alloys[15−17] and subsequently extending to ceramics,[18−20] oxides,[21−23] oxyfluorides,[10,24] borides,[19] carbides,[25,26] nitrides,[27] sulfides,[9] silicides,[28] and phosphides[29] over the past decade, underscores their versatile applicability. Recently, our group introduced a promising class of high-entropy Prussian blue analogues (HEPBAs).[30,31] These materials, belonging to the class of metal−organic frameworks (MOFs), facilitate the integration of the high-entropy approach into PBAs as sodium-ion battery (SIB) materials. HEPBAs exhibit fast charge/discharge kinetics and prolonged lifetimes compared to conventional PBA cathodes.[31] Characterized by the general formula $Na_xM[Fe(CN)_6]_y\square_{1-y}\cdot nH_2O$ (with $0 < x \leq 2$, $0 < y \leq 1$, M signifying transition-metal ions, $\square$ denoting $[Fe(CN)_6]$ vacancies, and n representing the H_2O content),[32−34] the tailorable positioning of M, ideally endowed with redox activity, underscores the utility of the high-entropy approach. Within the class of PBAs, three structural configurations are prominent, namely, cubic, monoclinic, and rhombohedral, with the latter two showing reduced symmetry compared to the cubic state.[35] Several HEPBAs composed of up to 6 metal atoms and also showing significantly improved electrochemical performance have been explored recently in subsequent studies.[31,36,37] However, the fundamental mechanisms underpinning the impact of the high-entropy configuration on the structure−property relationships remain elusive, particularly with regard to the influence on interrelation between configurational entropy and cationic redox processes in multicomponent hexacyanoferrate cathodes at high potentials. Prevailing investigations have predominantly concentrated on multicomponent PBAs cycled to cutoff potentials ≤4.2 V vs Na^+/Na. Notably, to the best of our knowledge, no study has undertaken a comparative assessment of the impact of configurational entropy on PBAs possessing distinct structures during high-voltage operation (>4.2 V vs Na^+/Na). It should be noted that high-voltage operation can induce structural distortion and cationic recombination, often in close relationship with irreversible phase transitions. In the context of PBAs, these phenomena manifest as a transformation from cubic to tetragonal phases upon charge to 4.2 V,[35,38] resulting in impeded kinetics and capacity decay.[37] Nevertheless, the more stable host structure of HEPBAs offers respite from lattice deformation and collapse, prerequisites for high-voltage operation, thereby improving cyclability. Hence, the key to suppressing structural degradation lies in the construction of a resilient host structure, characterized by robustness against high potentials.

In this work, we integrate disorder with crystal structure engineering, employing the high-entropy concept to modulate PBAs of distinct crystallographic configurations, achieved through meticulous control of reaction temperatures. The strategic integration of five metal species (Mn, Co, Fe, Ni, and Cu) yields two variants: cubic HEPBA, referred to as Cub-HEPBA, $Na_{1.46}Mn_{0.3}Co_{0.3}Fe_{0.133}Ni_{0.133}Cu_{0.133}[Fe(CN)_6]_{0.86}\square_{0.14}\cdot 1.74H_2O$, and a closely related monoclinic HEPBA, referred to as Mono-HEPBA, $Na_{1.48}Mn_{0.3}Co_{0.3}Fe_{0.133}Ni_{0.133}Cu_{0.133}[Fe(CN)_6]_{0.87}\square_{0.13}\cdot 1.12H_2O$. To elucidate the impact of the high-entropy concept on the different PBAs, various characterization techniques were employed, including *operando* X-ray diffraction (XRD), *in situ* differential electrochemical mass spectrometry (DEMS), *operando* electrochemical impedance spectroscopy (EIS), and *operando* stress analysis coupled with high-temperature performance studies and full cell testing. Through this multifaceted approach, we demonstrate the important role of high-entropy methods in improving the overall stability (of both cubic and monoclinic PBAs), with a profound impact from the selectivity of crystal structure, emphasizing that the

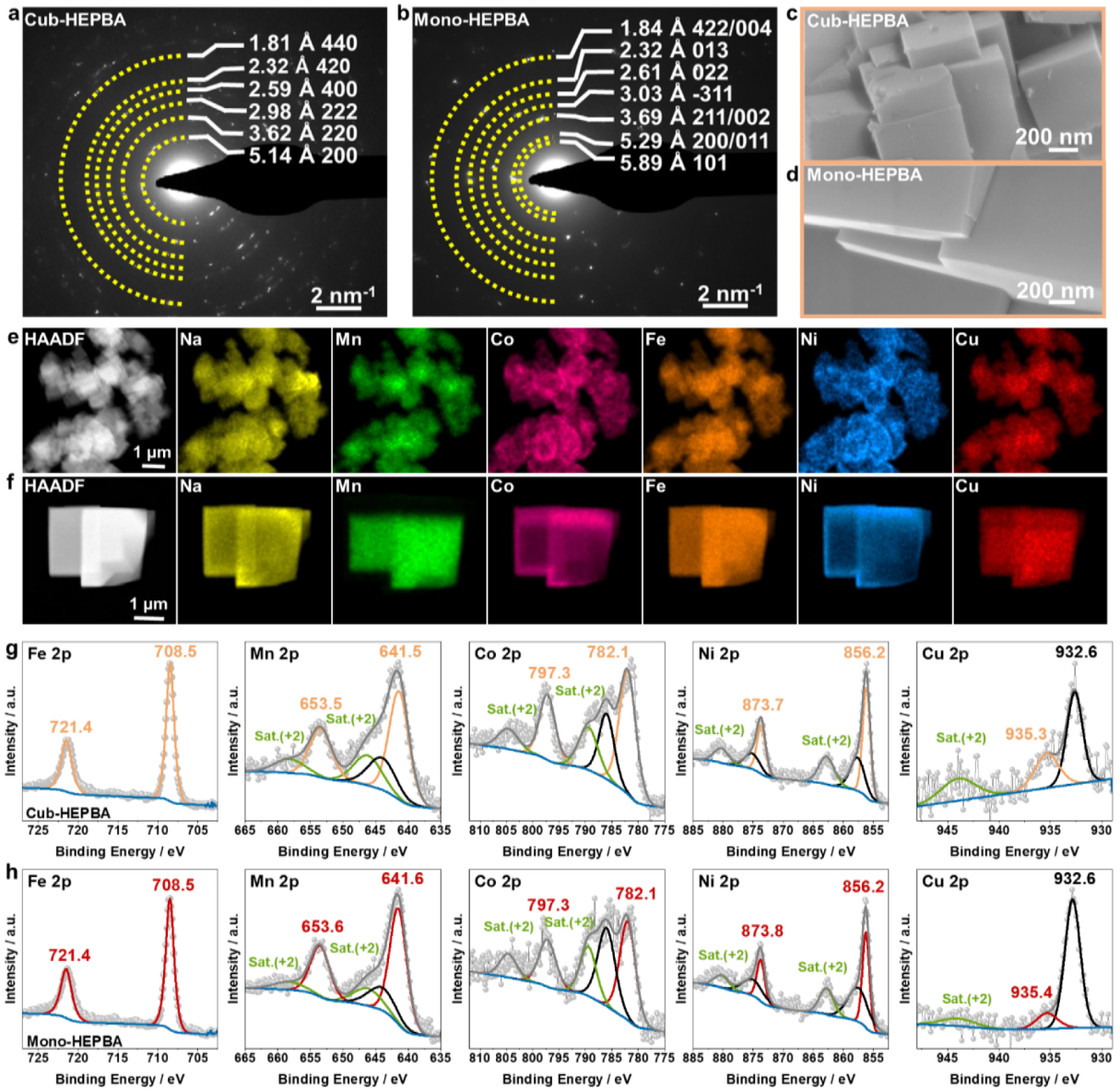

Figure 2. Structural and morphological characterization of Cub- and Mono-HEPBA. (a, b) SAED patterns, (c, d) SEM images, and (e, f) STEM-EDS elemental maps. (g, h) XPS analyses with detailed spectra of the Fe, Mn, Co, Ni, and Cu 2p core level regions.

integration of high-entropy and crystal-structure engineering enhances the performance of PBA frameworks as cathodes in SIB cells. The Cub-HEPBA with its robust structure exhibits excellent electrochemical performance, maintaining a specific capacity of about 60 mA h g^{-1} after 10000 cycles at 800 mA g^{-1}, characterized by high reversibility even under high-voltage conditions (4.5 V vs Na^+/Na). Conversely, the Mono-HEPBA, while delivering high capacities at low specific currents of ≤10 mA g^{-1}, manifests limitations when the C-rate is increased. The prevailing monoclinic structure exacerbates lattice distortions, resulting in compromised transport kinetics and degradation during cycling. This observation underscores the advantageous role of the highly symmetrical cubic structure in increasing stability and enhancing cyclability.

RESULTS AND DISCUSSION

In this study, two HEPBAs of similar composition but varying structure, namely, cubic vs monoclinic, are examined and compared. Through a straightforward approach of controlling reaction temperature, the integration of entropy and PBA crystal lattices has been achieved for tailored structural design. Specifically, the reaction temperature for the cubic phase was controlled at 25 °C, while for the monoclinic modification, it was maintained at 70 °C. The synthesis process is illustrated in Figure S1.

Structural Analysis. In a first step, XRD measurements and subsequent refinement analyses were performed to investigate the crystal structure and phase purity of the Cub- and Mono-HEPBA samples. The measurements confirmed the expected differences in crystal structures. Figure 1a shows that the structure of Cub-HEPBA conforms to the face-centered cubic lattice ($Fm-3m$, ICSD coll. code 193354),[39] with $a = b = c = 10.411(2)$ Å, $\alpha = \beta = \gamma = 90°$, and $V = 1128.5(8)$ $Å^3$, while Mono-HEPBA (Figure 1b) can be well indexed to a monoclinic structure of $P2_1/n$ space group[40] (ICSD coll. code 266392). The calculated lattice parameters for Mono-HEPBA are $a = 10.461(1)$ Å, $b = 7.484(1)$ Å, $c = 7.228(1)$ Å, $\beta = 91.36(1)°$, and $V = 565.7(1)$ $Å^3$. The major differences in the

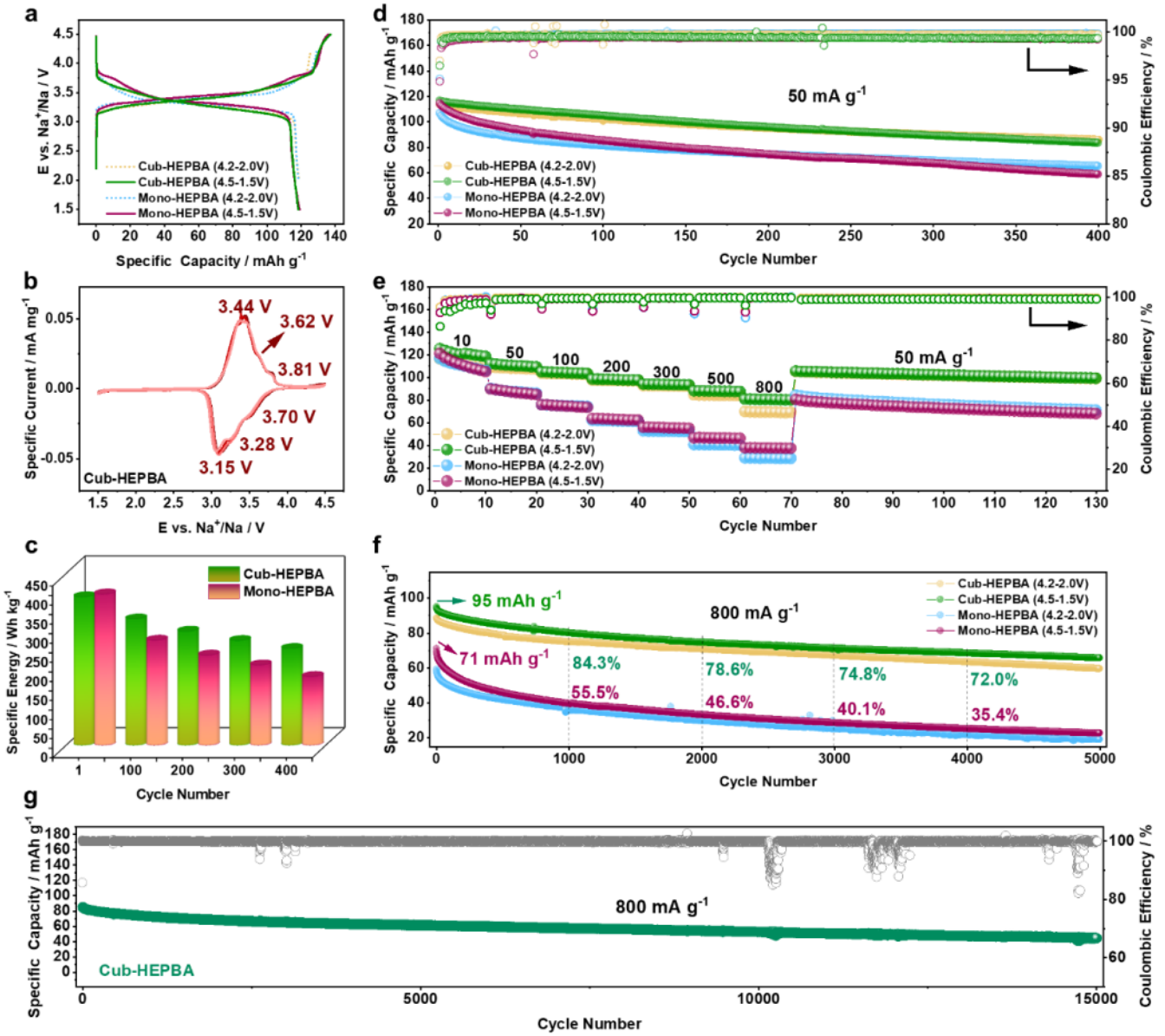

Figure 3. Electrochemical cycling of Cub- and Mono-HEPBA cells with cutoff potentials of 1.5 and 4.5 V or 2.0 and 4.2 V vs Na^+/Na. (a) Initial charge/discharge curves at 10 mA g^{-1}, (b) cyclic voltammograms of the first four cycles for Cub-HEPBA at 0.05 mV s^{-1}, (c) select specific energies (in the 1st, 100th, 200th, 300th, and 400th cycle), (d) cycling performance at 50 mA g^{-1}, (e) rate capability at specific currents ranging from 10 to 800 mA g^{-1}, and (f, g) cycling performance at 800 mA g^{-1} over 5000 and 15000 cycles.

XRD patterns are pronounced peak splittings observed for Mono-HEPBA at 18.7°, 19.1° (−211/211), 29.8°, 30.4° (031/013), and 37.8°, 38.7° (42−2/422), respectively. In contrast, no splitting of the reflections referring to the (200), (220), (400), and (420) crystal planes is apparent in the XRD pattern of Cub-HEPBA.[41,42] The results from the refinement of the structures are summarized in Tables S1 and S2. The structural analyses revealed a local atomic arrangement in which one of the five metal atoms (Mn/Co/Ni/Cu/Fe) is situated on the N-coordinated position. Specifically, in the Cub-HEPBA, the dominant metal species are Mn and Co, occupying the 4*b* sites, whereas in Mono-HEPBA, they are situated on the 2*a* sites. Concurrently, C-coordinated Fe ions (Fe_1) are found on the 4*a* sites for Cub-HEPBA and the 2*d* sites for Mono-HEPBA. Overall, the PBAs consist of linear chains of Fe_1−C≡N−M(Mn/Co/Ni/Cu/Fe_2)−N≡C−Fe_1 along the edges of the unit cell,[31,41] as illustrated in Figure 1c. It should be noted though that the monoclinic structure exhibits a tilt of the bond angles, i.e. −C≡N−M− is shifted from the typical 180° in the cubic phase to 159°. At the same time, the distance of Fe_1···M elongates from 5.205 Å (cubic) to 5.230 Å (monoclinic).

Inductively coupled plasma-optical emission spectroscopy (ICP-OES, Table S3) and differential scanning calorimetry (DSC, Figure S2) were employed to examine the chemical composition and water content of the as-synthesized materials. The chemical formulas were determined to be $Na_{1.46}Mn_{0.3}Co_{0.3}Fe_{0.133}Ni_{0.133}Cu_{0.133}[Fe(CN)_6]_{0.86}\square_{0.14}\cdot 1.74H_2O$ and $Na_{1.48}Mn_{0.3}Co_{0.3}Fe_{0.133}Ni_{0.133}Cu_{0.133}[Fe(CN)_6]_{0.87}\square_{0.13}\cdot 1.12H_2O$ for Cub- and Mono-HEPBA, respectively. From calculating the configurational entropy (ΔS_{conf}, see Supporting Information for details),[43] both

samples were found to have the same ΔS_{conf} of 1.53R, and therefore, can be classified as high-entropy PBAs.

Selected-area electron diffraction (SAED) (Figure 2a,b) was performed to further probe the structure of the samples. The (200), (220), (400), and (420) lattice planes of the cubic structure can be clearly observed for Cub-HEPBA, while the (101), (211), (022), and (013) planes of the monoclinic phase are apparent for Mono-HEPBA. As evidenced by scanning electron microscopy (SEM), in the case of Cub-HEPBA, relatively small cube-shaped particles form larger aggregates (secondary particles) characterized by an average size of 2 μm (Figure 2c). Mono-HEPBA also exhibits a cubic morphology, but with less pronounced aggregation (Figure 2d). Further characterization via scanning transmission electron microscopy (STEM) and energy dispersive X-ray spectroscopy (EDS) mapping corroborated the even distribution of Na, Mn, Co, Fe, Ni, and Cu in both samples (Figure 2e,f). In-depth analysis of the surface chemical composition was done using X-ray photoelectron spectroscopy (XPS). The relevant results are presented in Figures 2g,h and S3. The survey spectra collected from the Cub- and Mono-HEPBA samples (Figure S3a,b) confirm the presence of the aforementioned elements. Notably, the Na 1s spectrum of Cub-HEPBA features a single peak at a binding energy of 1071.8 eV (Figure S3c), in agreement with the data for Mono-HEPBA (Figure S3d). Comparison of the detailed spectra for the other metal species (Figure 2g,h) reveals that the results for Cub-HEPBA closely resemble those of Mono-HEPBA, with only minor binding energy shifts. For the Fe 2p region, a doublet at 708.5 and 721.4 eV is detected for both materials. It can be assigned to Fe^{2+} in the $[Fe^{2+}(CN)_6]^{4-}$ unit.[31,35,44,45] In contrast, the doublet of $[Fe^{3+}(CN)_6]^{3-}$ would be expected at higher binding energies (~710/723 eV).[37] Furthermore, the absence of other features suggests that the N-coordinated Fe ions are also in +2 oxidation state. The Mn 2p spectra show in both cases binding energies of the main $2p_{3/2}$ and $2p_{1/2}$ peaks of about 641.5 and 653.5 eV, in addition to distinct satellites at 646.4 and 658.3 eV. Furthermore, a broad Ni Auger peak is observed at ~644 eV. Because pronounced satellite structures are usually only found for Mn^{2+} compounds, the data suggest a main oxidation state of +2 for Mn in both HEPBAs.[30,46] Likewise, the Co 2p spectra display distinct satellite peaks at 789.6 and 804.8 eV, in addition to the main doublet at 782.1 eV ($2p_{3/2}$) and 797.3 eV ($2p_{1/2}$), along with a Fe Auger peak at ~786 eV.[30,31] Similar to Mn, the presence of satellite features points toward +2 oxidation state. In the case of Ni 2p, the main doublet at 856.2 eV ($2p_{3/2}$) and 873.7 eV ($2p_{1/2}$) is accompanied by another doublet at slightly higher binding energies of 857.6 and 875.3 eV, along with satellite features at ~863 and 880 eV.[31] The multiplet splitting renders it challenging to discern the Ni oxidation state. It is worth noting that the Ni $2p_{3/2}$ peak of NiO typically appears around 854 eV, while that of $Ni(OH)_2$ is detected at about 856 eV, a binding energy akin to that of Ni_2O_3.[47] Thus, determining the Ni oxidation state for the HEPBAs is challenging. Nevertheless, previous findings from normalized K-edge X-ray absorption near edge spectroscopy (XANES) hint at an oxidation state of +2.[31,37] Finally, the main peak in the Cu $2p_{3/2}$ region of Cub-HEPBA at 932.6 eV can be attributed to Cu^+.[30] Additionally, a smaller peak detected at a higher binding energy (935.3 eV), along with its corresponding shakeup satellite at 943.8 eV, suggests the presence of some Cu in +2 oxidation state,[10,48] consistent with observations made for Mono-HEPBA. The presence of Cu^+ indicates that an internal redox reaction (surface reduction) takes place during synthesis.[37]

Electrochemical Properties. Galvanostatic charge/discharge tests of Cub- and Mono-HEPBA cathodes at 10 mA g^{-1} revealed similar first-cycle specific discharge capacities of about 120 mA h g^{-1}, as displayed in Figure 3a, corresponding to specific energies of 396 W h kg^{-1} for Mono-HEPBA and 389 W h kg^{-1} for Cub-HEPBA. Closer examination of the voltage profiles unveiled a relatively high mean discharge voltage, attaining 3.32 and 3.30 V vs Na^+/Na for Mono- and Cub-HEPBA, respectively, along with a small voltage hysteresis of 0.2 V. In the cyclic voltammograms (Figures 3b and S4), the well-converged redox pairs at 3.44/3.15 V and 3.62/3.28 V correspond to the oxidation/reduction of C-coordinated Fe^{2+}/Fe^{3+} (low-spin, LS) and N-coordinated Mn^{2+}/Mn^{3+} (high-spin, HS), respectively.[30,32,49,50] Furthermore, the peaks at 3.81/3.70 V can be assigned to the Co^{2+}/Co^{3+} (HS) redox couple (i.e., Co bonded to the N atom of the CN^- ligands).[49,51] Notably, these redox pairs tend to merge into a single broad peak after four cycles, consistent with the attributes of HEPBAs described elsewhere.[30,31] The redox potentials in HEPBAs result from the complex interactions among the different metal ions and their specific coordination environments. These factors collectively dictate the electrochemical behavior observed in these materials.

As can be seen from the data shown in Figure 3c,d, the structural configuration has a profound effect on the cycling stability, with Cub-HEPBA being superior to Mono-HEPBA. This remains also true under the more demanding conditions of a wider electrochemical window (1.5–4.5 V). For instance, in the 100th, 200th, 300th, and 400th cycle at 50 mA g^{-1}, Cub-HEPBA delivered specific capacities of 105, 96, 89, and 84 mA h g^{-1}, respectively. In contrast, the capacity retention of Mono-HEPBA in the 400th cycle approached 51%, respective to a specific discharge capacity of only 59 mA h g^{-1}. The respective specific energies shown in Figure 3c (considering sodium metal as anode in a theoretical full cell) further underscore the beneficial effect of the cubic PBA structure on cyclability. Specifically, in the 300th and 400th cycle, Cub-HEPBA was capable of providing 275 and 254 W h kg^{-1}, respectively, while Mono-HEPBA only delivered 210 and 180 W h kg^{-1}. Comparative analysis of low-entropy PBAs (LEPBAs) with cubic and monoclinic structures (comprising equimolar amounts of Mn and Co, with ΔS_{conf} = 0.69R) emphasizes the much-improved cycling stability of Cub-HEPBA, both at low and high specific currents of 50 and 800 mA g^{-1}, respectively (Figure S5). This result demonstrates the positive effect of increased ΔS_{conf} on the electrochemical performance of multicomponent PBAs.

The superior cyclability of Cub-HEPBA was also evident when assessing the rate capability, as shown in Figure 3e. Cub-HEPBA delivered specific capacities of up to 81 mA h g^{-1} even at 800 mA g^{-1}. Furthermore, when the specific current was set to 50 mA g^{-1}, Cub-HEPBA exhibited a high specific capacity of 105 mA h g^{-1}. In contrast, Mono-HEPBA suffered from a substantial decrease in capacity with increasing current, approaching 38 mA h g^{-1} at 800 mA g^{-1}. It is also interesting to note that the specific capacity of Mono-HEPBA at 50 mA g^{-1} closely matches that of Cub-HEPBA at 800 mA g^{-1}. The different performance predominantly manifests at high rates, prompting the application of a high current for assessing the long-term stability. As shown in Figure 3f, Mono-HEPBA experienced a significant decline in capacity retention at 800

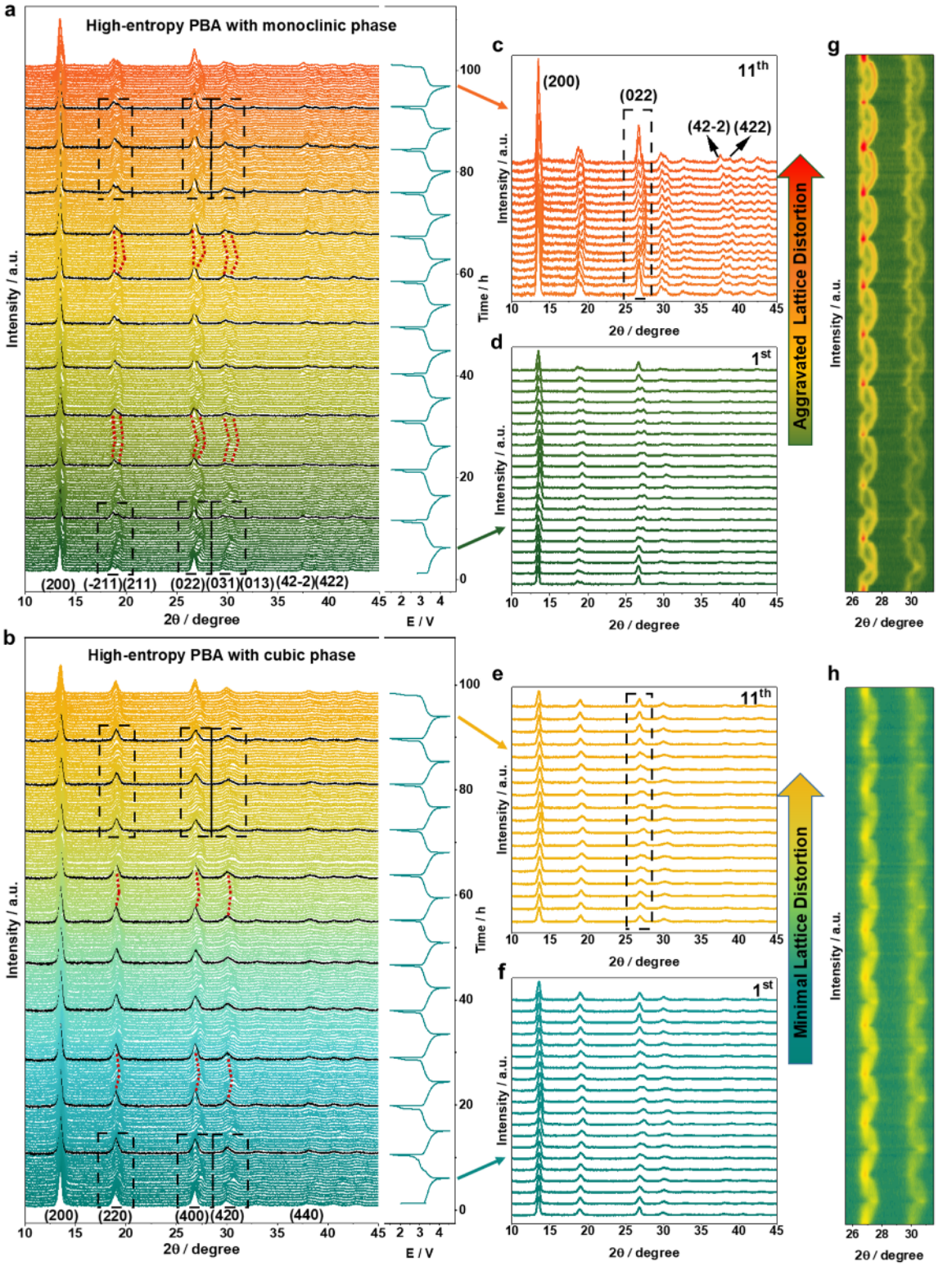

Figure 4. (a, b) *Operando* XRD characterization and corresponding voltage profiles of Mono- and Cub-HEPBA cathodes over 11 cycles at 25 mA g^{-1}. Select XRD patterns (first and 11th cycles) for (c, d) Mono-HEPBA and (e, f) Cub-HEPBA. (g, h) Closer view on the region between 25 and 32° in waterfall plots during cycling.

mA g^{-1}, from about 56% after 1000 cycles to 35% after 4000 cycles. In contrast, Cub-HEPBA demonstrated high stability, delivering a specific capacity of about 70 mA h g^{-1} (compared to 23 mA h g^{-1} for Mono-HEPBA) and showing a Coulomb efficiency of 99.97% (see Figures 3f and S6) even after more than 5000 cycles. Figure 3g displays the cycling performance of Cub-HEPBA over 15000 cycles at 800 mA g^{-1}, highlighting again the advantages of the cubic structure. Typically, structural degradation and cationic recombination tend to occur upon high-voltage operation, resulting in sluggish

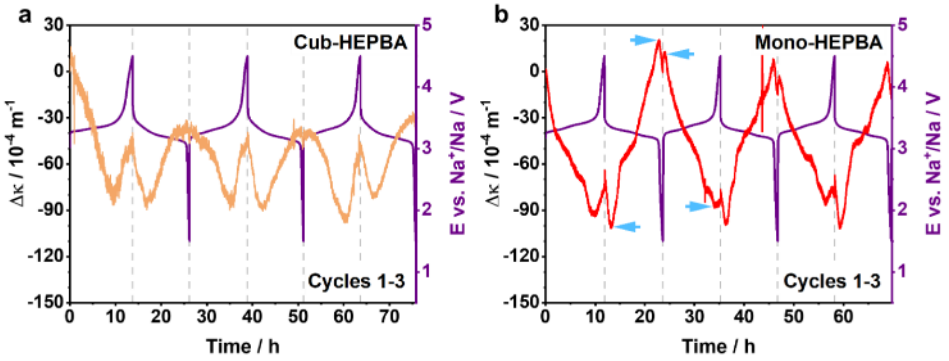

Figure 5. *Operando* curvature data and corresponding charge/discharge curves for (a) Cub-HEPBA and (b) Mono-HEPBA cathodes in the potential range between 1.5 and 4.5 V vs Na^+/Na at 10 mA g^{-1}.

kinetics and capacity decay,[30,52] in agreement with the performance decline observed for Mono-HEPBA. However, Cub-HEPBA still delivered specific capacities of about 60 mA h g^{-1} after 10000 cycles and showed minor capacity fading, despite the fast charge/discharge conditions and high upper cutoff potential of 4.5 V. Considering the morphological differences among the samples employed in this work, the aggregated primary particles of Cub-HEPBA result in a smaller surface-to-volume ratio, unlike the monocrystalline morphology of Mono-HEPBA. This apparently facilitates effective connectivity with the conductive carbon black and the current collector during prolonged cycling,[53] thereby enabling Cub-HEPBA to demonstrate stable and rapid sodium storage performance.

Electrochemical Mechanisms. To understand the origin of the electrochemical differences between cubic and monoclinic HEPBA, *operando* XRD investigations were carried out. The measurements were performed to follow the structural transformations during battery operation. The first patterns collected from the as-prepared materials in coin cells (Figure 4a,b) reassert the expected structures. The distinct peak splitting in Figure 4a, relating to the (−211/211), (031/013), and (42−2/422) reflections, is characteristic of monoclinic PBA materials, while the individual reflections seen for Cub-HEPBA in Figure 4b, namely, (200), (220), (400), (420), and (440) confirm the cubic structure. In the case of Mono-HEPBA, the applied current has a strong effect on the structural changes during cycling. *Operando* XRD measurements performed at a nominal specific current of 7 mA g^{-1} (Figure S7) revealed a profound structural transformation of the Mono-HEPBA. The characteristic peak splitting vanished upon cycling, and in addition to a single reflection denoting the (440) plane, new ones associated with the (200), (220), (400), and (420) planes appeared. This indicates the formation of a cubic structure when the cell is charged to 3.44 V vs Na^+/Na.[31,35,38] The latter structure remained until discharging to 2.9 V, whereupon it reverted back to the monoclinic structure [apparent peak splitting of (031/013) and (42−2/422)]. At low specific currents, Mono-HEPBA delivered similar specific capacities to Cub-HEPBA, even following the transition to a cubic phase. However, when the current is increased to 25 mA g^{-1}, Mono-HEPBA exhibited a markedly different structural evolution during Na^+ insertion/extraction, strongly impacting the electrochemical performance. The corresponding specific discharge capacities of Mono- and Cub-HEPBA at 25 mA g^{-1} achieved in the *operando* XRD measurements are given in Table S4.

While Figure 4d shows the absence of new reflections beyond the monoclinic structure during the initial cycle, obvious changes are apparent. First of all, a splitting of the (022) peak is observed as the Na^+ ions are extracted/inserted. In the following cycles, the peak splitting becomes increasingly pronounced, which is particularly evident from the fifth cycle onward. Detailed examination revealed a stronger splitting and increased intensity of the (022) reflection, as depicted in Figure 4c. Similarly, the intensity of the (200) reflection for Mono-HEPBA exhibited a 10-fold increase compared to its initial state. Also, the (42−2) and (422) reflections, which were less distinct in the first cycle, became substantially more pronounced by the 11th cycle. Simultaneously, the preexisting reflections corresponding to (−211/211) and (031/013) exhibited a stronger splitting. This is indicative of exacerbated deformation of the unit cell and degradation during successive cycling, and further helps explain the inferior electrochemical performance of Mono-HEPBA, as shown in Figure 3. In contrast, Cub-HEPBA demonstrated robust structural stability throughout cycling (Figure 4b). Specifically, when comparing the first and 11th cycle (Figure 4e,f), a solid-solution type behavior is observed,[30] characterized by minor reflection changes accompanied by modest broadening during de/sodiation. This highlights the high reversibility and minimal structural distortion, which can be attributed to a kind of quasi-zero-strain behavior.[54] The corresponding parameters derived from the refinement of structural models against the XRD patterns of Cub- and Mono-HEPBA are presented in Figure S8. The data corroborate the superior reversibility of redox processes in the case of Cub-HEPBA. Furthermore, waterfall plots of the *operando* XRD patterns provide evidence for the structural superiority of Cub-HEPBA. As depicted in Figure 4h, the cubic structure remained fully intact even after the 11th cycle. In contrast, Mono-HEPBA displayed evident structural deterioration from the fifth cycle onward (Figure 4g). This is indicative of its less robust nature when subjected to fast Na^+ extraction/insertion, and is further in agreement with the capacity fading observed for Mono-HEPBA at high C-rates.

In conclusion, while high specific capacities can be achieved with Mono-HEPBA at low currents, after a transition to the cubic phase during cycling, operation at higher C-rates leads to exacerbated lattice distortion. This underscores the advantage of the cubic structure, which promotes structural stability, and therefore, enhances performance. Owing to the robust structure optimized through the high-entropy approach, Cub-HEPBA clearly outperforms Mono-HEPBA in terms of rate capability and cycle life, among others.

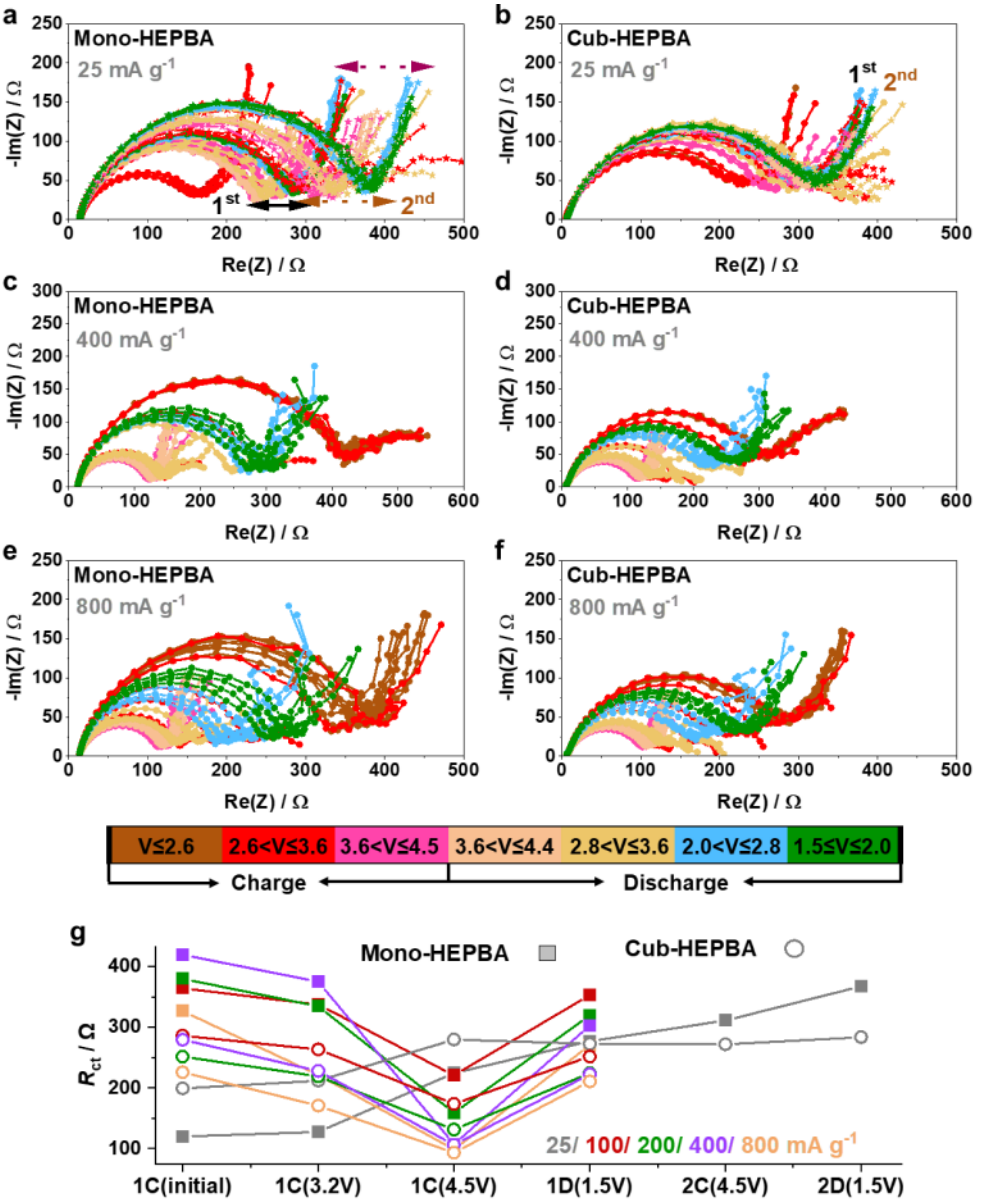

Figure 6. *Operando* **EIS analysis of the extraction/insertion of Na^+ from/into the HEPBAs cathodes at specific currents ranging from 25 to 800 mA g^{-1}. Nyquist plots for (a, c, e) Mono-HEPBA and (b, d, f) Cub-HEPBA. Different charge and discharge states are indicated by colored symbols and lines (see color code at the bottom). Note that data for the first two cycles are shown for 25 mA g^{-1}. (g) Comparison of R_{ct} between Cub- and Mono-HEPBA.**

The extraction and insertion of ions from/into an electrode can cause significant volume variations and mechanical stress. Here, *operando* stress analysis was performed via the substrate curvature method to investigate the mechanical stress evolution during cycling.[55] Both the Cub- and Mono-HEPBA samples showed similarities but also characteristic differences in their curvature data, as can be seen from Figure 5. For the Cub-HEPBA (Figure 5a), the curvature first decreases until it changes direction and shifts from compressive to tensile stress. This occurs at about 3.42 V vs Na^+/Na and coincides with the potential of the C-coordinated Fe^{2+}/Fe^{3+} redox couple. During the subsequent sodiation, a similar change in the direction of curvature/stress at about 3.31 V corresponds to the potential of the of N-coordinated Mn^{2+}/Mn^{3+} redox couple. The curvature of the cantilever oscillates upon cycling. However, at the cutoff potentials of 4.5 and 1.5 V, the curvature (or mechanical stress) reached similar levels. This suggests that Cub-HEPBA in the sodiated and desodiated states exerts similar forces on the current collector and passive components of the electrode. It also agrees with the negligible structural distortions observed by *operando* XRD, and further suggests that Cub-HEPBA may in fact be a zero-strain material. The characteristic shape of the curvature, as shown in Figure 5a, did not change within the 10 cycles that were performed. Aside from that, within individual cycles, it was relatively smooth and revealed no signs of abrupt volume changes or phase transitions. These observations may be a consequence of the robust structure of Cub-HEPBA, which helps explain its superior performance.

Although Mono-HEPBA exhibited trends similar to Cub-HEPBA, there were also deviations. For instance, in Figure 5b, the initial downward slope shows more pronounced features.

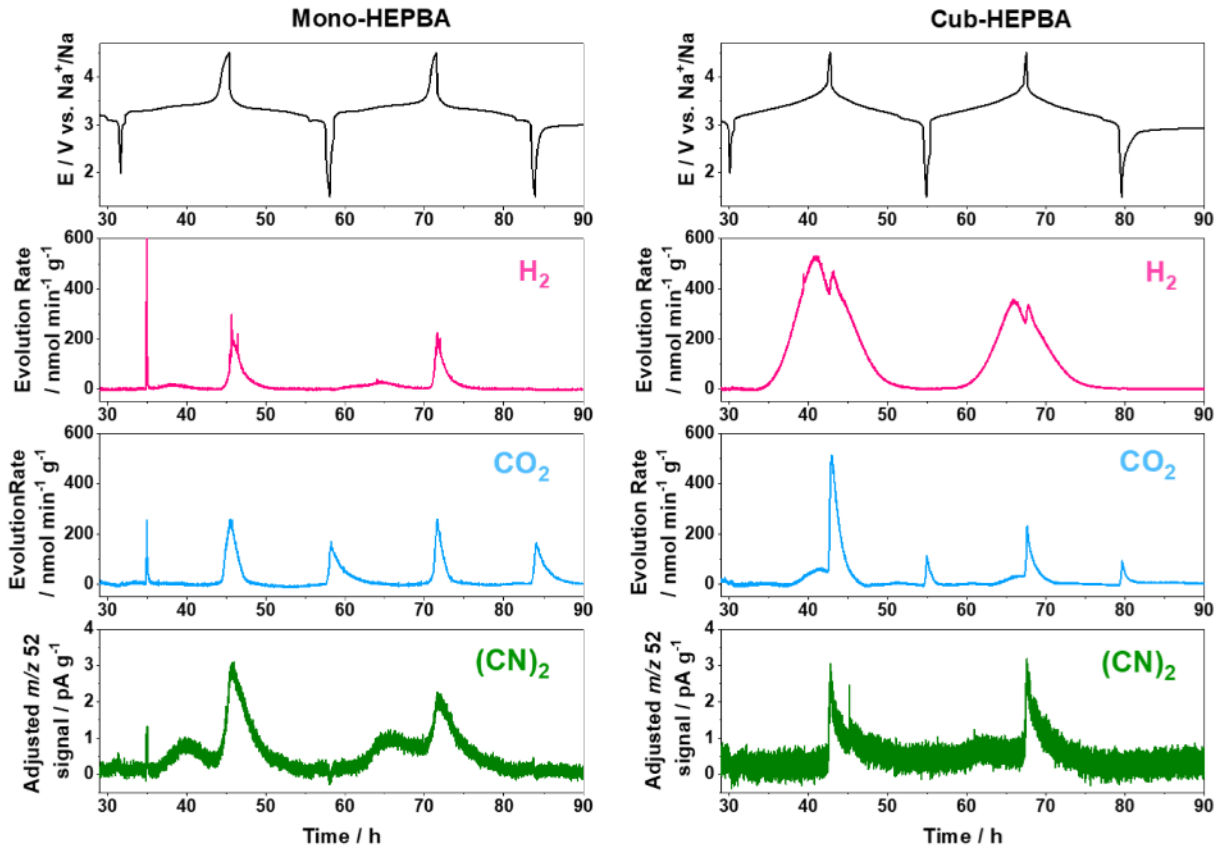

Figure 7. Gas evolution during cycling of Mono- and Cub-HEPBA cathodes in the second and third cycles, as determined via DEMS. The spike at 35 h in the Mono-HEPBA data is an artifact.

The small changes in slope may be caused by phase transitions. The first minimum of the curvature is reached around 3.5 V and matches with the structural change from monoclinic to cubic phase (Figure S7). As with Cub-HEPBA, Mono-HEPBA changes its direction of curvature, and the stress in the electrode shifts from compression to tension. When comparing Figure 5a,b, it can be seen that the curvature amplitude of this change is quite weak for Mono-HEPBA. In particular, the curvature or stress levels for Mono-HEPBA were not similar before and after sodiation. In the sodiated state, the electrode is more tensile than in the desodiated state. Despite similar capacities, the amplitude of the curvature oscillation during cycling was about twice as high as for Cub-HEPBA. This may be attributed to major changes in the lattice parameters of Mono-HEPBA during the extraction and insertion of Na^+ ions, as shown in Figure 4a, resulting in more distinct features in the curvature data. Symmetric reaction pathways are reflected by a mirror symmetry in curvature around the fully sodiated and desodiated states (see dashed lines in Figure 5). For Mono-HEPBA, the Na^+ extraction/insertion mechanism appears to be less symmetrical due to the fine features that differ between both states (marked by arrows in Figure 5b). Moreover, the features found in the curvature data for Mono-HEPBA slightly change from cycle to cycle. This seems to be indicative of structural degradation, such as particle rearrangements and/or binder/carbon black motion.

To examine the impact of the different structures on impedance, *operando* EIS measurements were conducted on the Mono- and Cub-HEPBA cathodes for a range of specific currents (25, 100, 200, 400, and 800 mA g^{-1}). As evident from Figures 6 and S9, the spectra exhibit characteristic features, comprising a semicircle at high frequency and a straight line at low frequency.[56] The semicircle is related to the charge-transfer resistance (R_{ct}), and the sloping line reflects the diffusion impedance.[57−59] Selected spectra were further fitted using the equivalent circuit shown in Figure S10. A comparative analysis of the first and second cycles at 25 mA g^{-1} revealed a notable increase in the semicircle for Mono-HEPBA (Figure 6a), signifying an increased R_{ct}, from 277 to 368 Ω at the fully discharged state (Table S5). In contrast, Cub-HEPBA revealed no substantial change in resistance after two cycles at 25 mA g^{-1} (Figure 6b), maintaining at ∼280 Ω at 1.5 V vs Na^+/Na (Table S6), indicative of high reversibility. The change in resistance did not follow a clear trend (continuous increase) when testing the cells at higher specific currents. Both materials showed a higher R_{ct} when operated at ≤3.6 V than when cycled in the potential range between 3.6 and 4.5 V during desodiation at 100, 200, and 400 mA g^{-1} (Figures S9 and 6c, d). This is because oxidation processes associated with the C-coordinated Fe^{2+}/Fe^{3+} and N-coordinated Mn^{2+}/Mn^{3+} couples are mainly involved in this potential window.[57] Obviously, the R_{ct} is always much higher for Mono-HEPBA than Cub-HEPBA before charging to 3.6 V. For instance, R_{ct} values of 338, 335, and 376 Ω were found for Mono-HEPBA at 3.2 V for specific currents of 100, 200, and 400 mA g^{-1}, respectively, while the corresponding values for Cub-HEPBA under the same conditions are 264, 219, and 228 Ω, as summarized in Figure 6g. This result suggests that the increase in cathodelelectrolyte interfacial resistance is mitigated in Cub-HEPBA, which is probably related to its more robust

structure. In addition, the smaller primary particle size appears to facilitate charge transfer across the interface.[53] For both cathodes, higher resistances were observed near the end of discharge (2.8−1.5 V), compared to other states of discharge, revealing that full reinsertion of Na^+ is unfavorable. However, the smaller R_{ct} of Cub-HEPBA observed consistently (Figure 6g), also in the range of 2.8−1.5 V, indicates that the cubic structure is electrochemically better accessible.

Interestingly, there was no distinct change in resistance for the Cub-HEPBA when increasing the specific current from 25 to 400 mA g^{-1}, implying that the material is not susceptible to unfavorable side reactions that are otherwise easily triggered at high C-rates and/or high/low potentials.[58] By contrast, an increase in specific current induces distinct lattice distortion of the monoclinic structure, as verified by the *operando* XRD analysis (Figure 4a), resulting in compromised transport kinetics and exacerbated degradation throughout cycling. Major differences in impedance between Mono- and Cub-HEPBA were also observed when applying 800 mA g^{-1} to the cells, as displayed in Figure 6e,f. Notably, the R_{ct} for Cub-HEPBA was much lower than that of Mono-HEPBA over the whole cycle. Mono-HEPBA suffered from strong variations in resistance, from 327 Ω in the initial state to 99 Ω at 4.5 V, and then to 271 Ω upon discharge to 1.5 V, compared to 226, 93, and 211 Ω, respectively, for Cub-HEPBA. It can be speculated that this is due to the more robust structure of Cub-HEPBA, allowing for facile charge transport even under harsh conditions.

The evolution of gases from both cathode materials during cycling was studied *in situ* via DEMS, utilizing a customized open headspace cell setup.[60−62] Moisture and coordinated water commonly lead to H_2 (m/z = 2) formation, while surface carbonates and electrolyte decomposition result in CO_2 (m/z = 44) evolution.[63,64] In oxide cathode materials, both for sodium- and lithium-ion batteries, the release of O_2 by oxidation of lattice oxygen at high states of charge additionally contributes to gas evolution, and by oxidation of the electrolyte, also to the formation of CO_2.[65,66] In hexacyanoferrate cathodes, on the other hand, as we have shown previously, cyanide anions can be oxidized to form gaseous cyanogen [$(CN)_2$, m/z = 52] upon charge, thus degrading the active material, especially in the presence of $NaClO_4$.[30,37,62] The gas evolution of Cub- and Mono-HEPBA is depicted in Figure 7 for the second and third cycles, measured in a potential range of 1.5−4.5 V vs Na^+/Na. In the first cycle, the potential window was restricted to 2.0−4.2 V. The observed gas evolution over the whole measurement range is shown in Figure S11. Table S7 reports the evolved gas amounts, i.e., curve integrals, and specific capacities for each cycle and material.

Due to their innate water content, significant H_2 evolution is expected for hexacyanoferrates.[30,37] As coordinated water is released mostly near the end of charge and in the form of $Na(OH_2)^+$, the H_2 evolution rate increases at higher potentials.[62,67,68] For Cub-HEPBA, an earlier onset of H_2 evolution as well as a higher total H_2 amount, when compared to Mono-HEPBA, are observed. In addition, the highest evolution rate in the first cycle is not observed at the end of charge, but around 3.5 V, indicating that release of lattice water is contributing to the H_2 evolution. The latter appears to be present only to a much lesser extent in Mono-HEPBA, where the H_2 evolution is restricted to smaller amounts around the end of charge. The findings are in good agreement with the difference in water content of both materials (Table S3). However, an influence of the smaller particle size and higher specific surface area of Cub-HEPBA on water release of the materials cannot be ruled out. A dent-like decrease of H_2 evolution rate in Cub-HEPBA when charged to 4.5 V is likely due to H_2 being partially displaced by the strong CO_2 evolution setting in at this point.[62] Strong CO_2 evolution occurs due to electrochemical electrolyte oxidation at potentials above ∼4.3 V, equal to ∼4.6 V vs Li^+/Li, the stability limit for organic carbonates, such as ethylene carbonate (EC).[65] Before this onset, a weaker evolution of CO_2 is observed for Cub-HEPBA, and as it is concurrent with the H_2 evolution, i.e., water release, stems from hydrolysis of EC under release of CO_2.[62,69−71] While the electrochemical electrolyte oxidation is not dependent upon the cathode material, as evident from similar CO_2 evolution from both materials in the third cycle, the higher CO_2 evolution of Cub-HEPBA in the first two cycles can be attributed again to a higher water content in the material, as shown previously.[62] Finally, further CO_2 evolution independent of cathode material was observed near the end of discharge when going below 2.0 V. This was previously found to be due to reduction of fluoroethylene carbonate in the electrolyte at low potentials.[72,73]

The evolution of $(CN)_2$ has previously been reported both during thermal runaway of Prussian white (PW) cells and during charge.[30,37,62,74] A direct quantification of $(CN)_2$ evolution via DEMS was not possible due to a lack of suitable calibration gas mixtures needed for the conversion of ion currents recorded in the mass spectrometer to concentrations in the gas mixture. In the case of $(CN)_2$, no such calibration curve can be obtained, thus the measured detector currents (m/z = 52) are reported, still allowing for a semiquantitative analysis.[60,61] To compare the gas evolution between different measurements, changes in the secondary electron multiplier (SEM) gain (between the measurements) have to be considered, and if necessary, compensated for. The gain decreases over time due to aging and degradation, with the effect most pronounced in newly installed SEMs, although it can be roughly compensated for by applying a higher voltage.[75,76] Since H_2 and CO_2 are part of the calibration gas mixture, a relative comparison of SEM gain can be made from the calibration curve slopes of these gases, as outlined in Figure S12 and Table S8. For a fair comparison of evolution rates, the $(CN)_2$ raw signal is then adjusted by the factor between these calibration slopes and normalized by electrode weight. This corrected signal is depicted in Figures 7 and S11. A more detailed report of experimental considerations in the DEMS study of hexacyanoferrates can be found in the literature.[62] Therein, we have also demonstrated that, while the water content of the cathode material determines the H_2 evolution, the conductive salt determines the evolution of CO_2 and $(CN)_2$. $NaClO_4$, as used herein, results in the necessary electrolyte basicity for hydrolysis of EC under CO_2 evolution to occur and increases the $(CN)_2$ evolution rate, associated with the formation of a cathode electrolyte interphase (CEI) due to its oxidative properties. The $(CN)_2$ evolution rate of a given phase or material is therefore inversely related to its stability against oxidation (by reactive ClO_x species).

In this work, in all cycles, the major difference in $(CN)_2$ evolution profiles between the two samples is the occurrence of a shoulder peak in Mono-HEPBA, which is especially strong in the initial cycle and absent in Cub-HEPBA. Furthermore, in

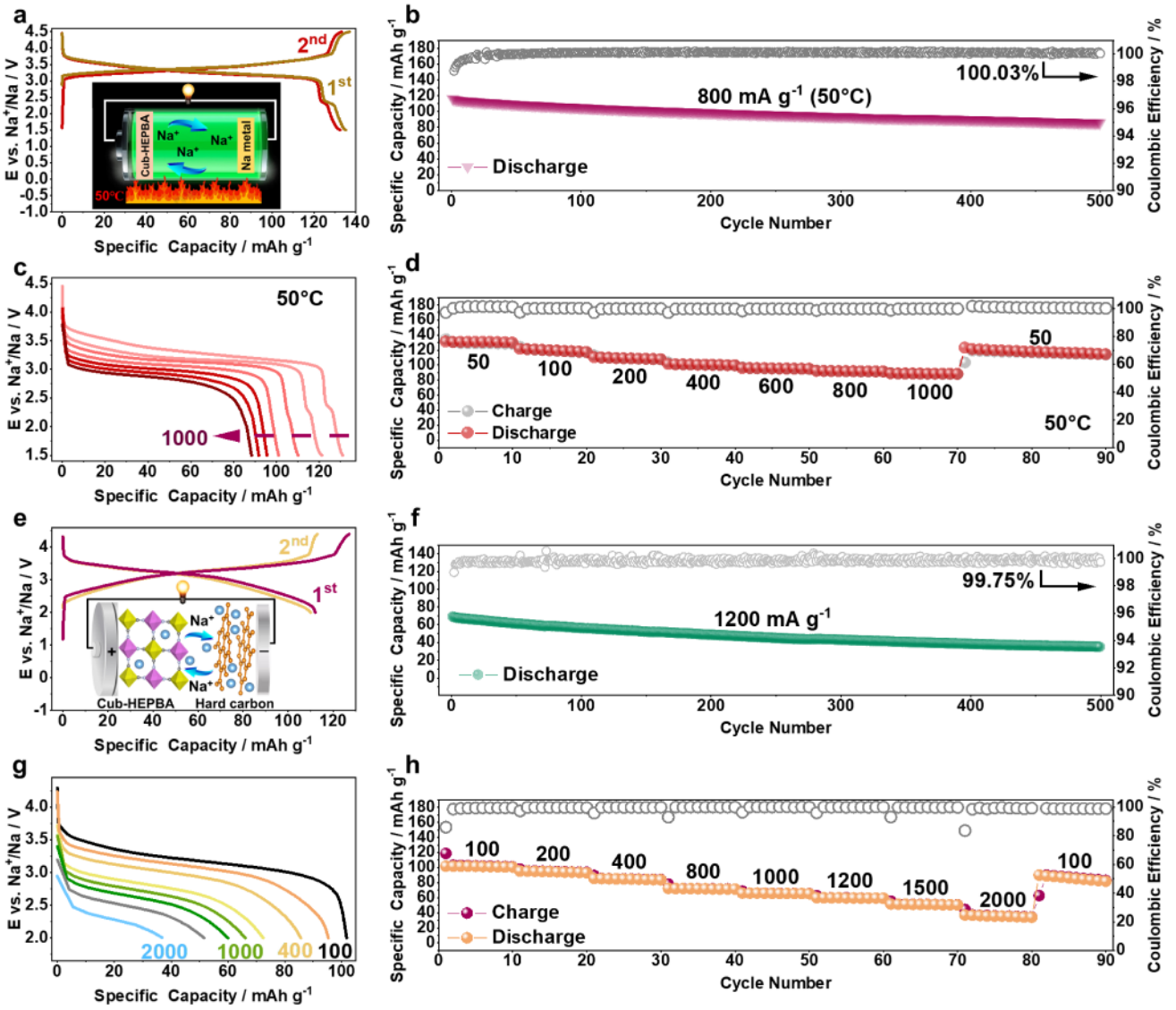

Figure 8. (a–d) Cyclability of Cub-HEPBA cathodes at 50 °C. (a) Voltage profiles at 50 mA g^{-1} of the first two cycles, (b) long-term cycling performance at 800 mA g^{-1}, and (c, d) initial discharge curves at specific currents ranging from 50 to 1000 mA g^{-1} and corresponding rate capability. (e–h) Na-ion full cell performance of Cub-HEPBA in the 2.0–4.4 V range. (e) Voltage profiles of coin cells at 20 mA g^{-1} of the first two cycles, (f) long-term cycling performance at 1200 mA g^{-1}, and (g, h) initial discharge curves at specific currents ranging from 100 and 2000 mA g^{-1} and corresponding rate capability.

the second and third cycles, the evolution curves appear to be narrower for Cub-HEPBA. Yet, as evident when extrapolating evolution rates over potential, as shown in Figure S13, this is only due to the slightly different shape of the voltage profiles at the end of charge, while at any given potential above the observed peak shoulder, the $(CN)_2$ evolution rate is similar between both materials. This is also reflected in similar peak integrals, as shown in Table S7. In a previous study of low- and high-entropy PW cathodes, a peak shoulder during charge was observed only in the low-entropy material and explained by a phase transition.[37] Gas evolution during the phase transition was attributed to concurrent degradation mechanisms, such as surface destabilization or formation of cracks leading to exposure of additional surfaces, and possibly cyanide-containing surface impurities, to the electrolyte. In the previous study, simultaneous to the phase transition and $(CN)_2$ evolution, also H_2 evolution was observed. Because of the overall stronger H_2 evolution in this work, due to the higher cutoff potential and the materials, especially Cub-HEPBA, this is not clearly visible in Figure 7, but as shown in Figure S14, concurrent H_2 evolution is in fact observed for Mono-HEPBA. With these findings considered, the peak shoulder around 3.4 V seen for Mono-HEPBA is likely again a result of the transition to the cubic phase.

Other than the different potential window applied, the main difference between the previous study and this work is the composition of the materials. Previously, a low-entropy PW was compared to a high-entropy PW, with the difference in configurational entropy resulting from different compositions. By contrast, in this work, both materials differ only marginally in their composition, but in their preparation and resulting crystal structure. In analogy to the previous study, the $(CN)_2$ evolution rate first peaks during the phase transition of Mono-HEPBA, but then is similar for the Cub- and Mono-HEPBA samples once the transition has occurred, as expected for materials having the same phase and composition then. In

contrast, materials of different composition resulted in different $(CN)_2$ evolution rates, i.e., different material stability against oxidation.[37,62]

Taken together, Mono-HEPBA exhibits a more substantial evolution of $(CN)_2$ compared to that of Cub-HEPBA, which we attribute to the additional release during the phase transition at ~3.44 V vs Na^+/Na, suggesting structural degradation as a consequence. This result once again emphasizes the significance of integrating disorder (entropy) with crystal structure optimization in electrode engineering.

High-Temperature Stability and Full Cell Performance. Since thermal stability is a crucial factor in the safety requirements of SIBs, the electrochemical performance of Cub-HEPBA at elevated temperature was studied in this work as well. Figure 8a shows the charge/discharge curves of the first two cycles at 50 °C. The Cub-HEPBA cathode delivered a high specific discharge capacity of 135 mA h g^{-1}, corresponding to a specific energy of 436 W h kg^{-1}. The reactivity of the LS- and HS-Fe redox couples was evidently higher at 50 °C, as indicated in Figure S15a. Notably, benefiting from the robust structure, Cub-HEPBA revealed an excellent sodium-storage ability both in terms of cycling stability and rate performance at elevated temperature. More specifically, a reversible specific capacity of ~90 mA h g^{-1} after 500 cycles at 800 mA g^{-1} was achieved (Figures 8b and S15b). The Cub-HEPBA cathode also exhibited good rate capability. As evident from Figure 8c,d, even at the highest applied specific current of 1000 mA g^{-1}, it was still capable of delivering a specific discharge capacity of 90 mA h g^{-1}. This suggests that, compared with most of the conventional hexacyanoferrates reported in the literature,[53,77] the introduction of compositional disorder (configurational entropy) positively affects the stability and cycling performance at elevated temperature.

To evaluate the practical applicability, full cells were fabricated with the Cub-HEPBA as cathode material and hard carbon as anode material. In this case, the calculation of specific capacities and energy densities was done based on the mass of Cub-HEPBA. To activate the hard carbon anode, it was initially cycled at 10 mA g^{-1} for two cycles between 0.02 and 2.0 V vs Na^+/Na in Na-metal cells, and then charged to 0.5 V and harvested (Figure S16). As shown in Figure 8e, the Cub-HEPBA full cell delivered an initial specific discharge capacity of 112 mA h g^{-1} at 20 mA g^{-1}, corresponding to a specific energy of 345 W h kg^{-1} (mean discharge voltage of 3.1 V). Stable electrochemical performance was also observed when applying high specific currents, as shown in Figures 8f–h and S17. For instance, at 100, 400, 1000, and 2000 mA g^{-1}, the Cub-HEPBA full cell was still capable of delivering 102, 86, 66, and 37 mA h g^{-1}, respectively. Overall, the results clearly demonstrate that cubic HEPBAs are promising candidates for application in SIBs, especially for the development of fast-charging cells.

CONCLUSIONS

In the present work, compositional disorder was introduced into Prussian blue analogue (PBA) cathode materials with distinct structural differences to study the effect that configurational entropy has on cycling performance. Cubic and monoclinic HEPBAs with similar configurational entropy, stoichiometry, and elemental composition, were systematically investigated to analyze their cyclability in Na-ion cells. The cubic HEPBA was found to benefit from improved structural attributes, leading to high reversibility, good thermal stability, and enabling extended cycle life, even under high-voltage operation. Therefore, it holds promise for application as positive electrode in rechargeable Na-ion cells, especially for fast-charging batteries. By contrast, monoclinic HEPBA showed strongly impaired performance, indicating that the original structure is crucial for cycling, independent of stoichiometry and configurational entropy. Overall, this work is highlighting the preference of highly symmetrical, high-entropy battery materials and further emphasizes the intricate relationship between structure and performance.

EXPERIMENTAL SECTION

Synthesis. Cubic and monoclinic, high-entropy $Na_xMn_{0.3}Co_{0.3}Fe_{0.133}Ni_{0.133}Cu_{0.133}[Fe(CN)_6]_{1-y}\cdot nH_2O$ materials were prepared by a simple coprecipitation method at different temperatures. Typically, 8 mmol $Na_4Fe(CN)_6\cdot 10H_2O$ and stoichiometric amounts of $FeCl_2\cdot 4H_2O$, $MnCl_2\cdot 4H_2O$, $NiCl_2\cdot 6H_2O$, $CuCl_2\cdot 2.5H_2O$, and $CoCl_2\cdot 6H_2O$ (in total 6 mmol metal precursors) were dissolved in 100 mL deionized water to form solutions A and B. After complete dissolution (ultrasonication for 0.5 h and then stirring for 0.5 h), sodium citrate (5.35 g) was added under stirring to obtain homogeneous solutions. Then, the two solutions A and B were slowly and simultaneously added dropwise to 200 mL deionized water under stirring to form solution C. The mixture was kept stirring for 4 h at room temperature for Cub-HEPBA and at 70 °C for Mono-HEPBA, and aged for 12 h without stirring before centrifugation. The precipitate was washed several times with deionized water, and the wet powder was finally dried in a vacuum oven at 100 °C for 12 h. To prevent the samples from water uptake, they were quickly transferred into an Ar glovebox.

Electrochemical Measurements. Cathodes were made from the active compounds (70 wt %), Super C65 carbon black (TIMCAL, 20 wt %), and polyvinylidene difluoride (PVdF, Solef 5130, Solvay, 10 wt %) dispersed in *N*-methyl-2-pyrrolidone (NMP, Sigma-Aldrich) using a Thinky ARE-250 blender (two times, each for 3 min). The resulting slurries were uniformly spread onto Al foil by a laboratory doctor blade (150 μm wet-film thickness), and then dried under vacuum at 120 °C for 24 h. Circular electrodes of diameter 13 mm were punched out and further dried for 10 h at 120 °C. The loading of active material was in the range of 1.4–1.6 mg cm^{-2}. The specific energy of the cells was calculated from the mean voltage and the specific capacity.

Galvanostatic testing was carried out on a LAND CT3001A battery system (Wuhan LAND Electronic Co. Ltd.) using standard CR2032 coin cells with cutoff potentials of 1.5 and 4.5 V, as well as 2.0 and 4.2 V vs Na^+/Na. Sodium metal was used as counter and reference electrode, glass microfiber filter (GF/D, Whatman) as separator, and 1 M $NaClO_4$ in ethylene carbonate:dimethyl carbonate:propylene carbonate (EC:DMC:PC, 1:1:1 by vol.) with 5 vol % fluoroethylene carbonate (FEC) as electrolyte. All cells were assembled in an Ar glovebox (MBraun UNIlab, $[H_2O]$ and $[O_2]$ < 0.1 ppm).

Cyclic voltammetry measurements were carried out using a BioLogic VSP-300 potentiostat in the potential range from 1.5 to 4.5 V vs Na^+/Na.

Major electrochemical measurements were performed in climatic chambers with a set temperature of 25 (±1) or 50 (±1) °C.

Full Cell Fabrication. The cathode was prepared from Cub-HEPBA, Super C65, and PVDF (7:2:1 weight ratio) on Al foil, as described above. The anode was fabricated by spreading a slurry of hard carbon, Super C65, and PVDF (8:1:1 weight ratio) onto Cu foil. To activate the anode, the hard carbon was initially cycled for two cycles at 10 mA g^{-1} between 0.02 and 2.0 V vs Na^+/Na in a Na-metal cell and then charged to 0.5 V to obtain the precycled anode for assembling the Cub-HEPBA|hard carbon full cell. The mass ratio of Cub-HEPBA to hard carbon was calculated to be 2:1. The specific capacities and energy densities were calculated based on the mass of Cub-HEPBA.

Characterization. X-ray diffraction (XRD) patterns of the samples were collected using a STOE Stadi P diffractometer equipped with a Ga-jet X-ray source (Ga−K_β radiation, λ = 1.20793 Å) in the 2θ range of 10−55°. Rietveld refinement analyses were performed using TOPAS Academics V5 software.

Inductively coupled plasma-optical emission spectroscopy (ICP-OES) measurements were carried out on a SPECTRO ARCOS SOP instrument.

Differential scanning calorimetry (DSC) measurements were performed at heating and cooling rates of 5 °C min^{-1} under Ar atmosphere using a NETZSCH DSC 204F1 Phoenix. The content of crystal water was estimated from the weight loss in the temperature range of 40−130 °C. For this purpose, the specific enthalpy of dehydration was used, which can be estimated as follows: $\Delta H = \int_{t1}^{t2} \frac{q}{m}\,dt$, where q, m, and t represent the heat flux (mW), mass (mg), and time (s), respectively.[78,79] The molar enthalpy of dehydration is estimated to be 15.81 kJ mol^{-1}.[79] The total molar content in the measured sample ($n_{H_2O,total}$) is estimated according to $n_{H_2O,total} = \frac{\Delta H}{15.81 * 1000}$. Then, the content of crystal water per mol is derived from $n_{H_2O,total} = \frac{m_{sample}}{M_{sample}} * x$, where m is sample mass (g) and M_{sample} represents the molar mass (g mol^{-1}). The M_{sample} is calculated via $M_{sample} = M_{without\ crystal\ water} + xM_{H_2O}$.

The sample morphology was characterized by scanning electron microscopy (SEM, Zeiss LEO 1530) and transmission electron microscopy (TEM). High-angle annular dark-field (HAADF) scanning TEM (STEM) measurements were performed on a Thermo Fisher Themis Z equipped with a probe-corrector (S-CORR) at 300 kV. The elemental distribution was studied by drift-corrected elemental mapping using a Thermo Fisher Super-X energy-dispersive X-ray spectroscopy (EDS) detector.

X-ray photoelectron spectroscopy (XPS) measurements were conducted on a PHI 5800 MultiTechnique ESCA system using monochromatic Al−K_α radiation (300 W, 15 kV), a takeoff angle of 45°, and pass energies at the electron analyzer of 29.35 eV for detailed scans and 93.9 eV for survey scans. Sample charging effects were relatively small, thus neutralization was not necessary. The main C 1s peak at 284.8 eV was used for calibration of the binding energy. Peak fitting was done with CasaXPS using Gaussian−Lorentzian peak shapes. For the peak fitting of the transition-metal 2p doublets, the expected intensity ratio of 2:1 and spin−orbit splitting were used.

***Operando* XRD.** The structural evolution of the samples was investigated using a STOE Stadi P diffractometer equipped with a Ga-jet X-ray source (Ga−K_β radiation, λ = 1.20793 Å) in transmission mode. To this end, electrodes with higher areal loading of active material (~5 mg cm^{-2}) were employed, along with customized coin cells with Kapton windows of 4 mm diameter. The galvanostatic cycling was accomplished by a SP-150 potentiostat/galvanostat (BioLogic) at specific currents of 7 and 25 mA g^{-1}.

***Operando* Electrochemical Impedance Spectroscopy (EIS).** EIS measurements were performed using a BioLogic VSP-300 potentiostat in the potential range of 1.5−4.5 V vs Na^+/Na at specific currents ranging from 25 and 800 mA g^{-1}. Impedance spectra were recorded at all even potentials (1.6, 1.8, 2.0 V,···), as well as in fully charged (4.5 V) and discharged states (1.5 V) during cycling, in the frequency range from 100 kHz to 1 Hz.

***Operando* Stress Analysis.** *Operando* curvature measurements were conducted using a customized substrate curvature cell. The HEPBA electrodes were glued onto 15 mm × 4 mm borosilicate glass cantilevers of thickness 155 μm. The cantilevers consist of four layers (substrate|glue|current collector|composite electrode) and are clamped into the test cells. The clamp affixes the cantilever and ensures electrical contact by pressing it onto a contact region within the cell. Curvature measurements were performed at a distance from the clamp to avoid stress irregularities due to mechanical constraints caused by the clamping force. Mechanical stress within the composite electrode leads to a response of the four-layer cantilever in the form of curvature. To measure the radius of curvature, two laser beams were used. They enter and leave the cell through a window and are reflected at the backside of the cantilever. The angle between the laser beams was tracked by a CMOS camera[55,80] and measured as a distance between two spots on the camera. This distance linearly correlates with the radius of the cantilever. The curvature is the inverse of this radius, and for thin layers on rigid thick substrates, the curvature is directly proportional to the mechanical stress within the thin layer (Stoney's relation) according to[81] $\Delta\kappa = \frac{1}{r_1} - \frac{1}{r_0} = \frac{\Delta d}{2 * L * l}$. In this equation, $\Delta\kappa$ is the change in curvature (the inverse of the radius of curvature) and can be determined from the change in displacement of the distance d between the two laser spots on the camera. L is the distance between the camera sensor and the cantilever, and l represents the distance between the two laser spots on the cantilever. r_0 corresponds to the radius at the start of the measurement and $1/r_0$ is subtracted from the curvature to achieve zero curvature (stress/volume change) at the beginning. Here, we deal with a multilayer system and a thick active film consisting of a composite material.[80] Stoney's relation[81] cannot be used, and it is therefore not readily possible to directly relate curvature and stress. Nevertheless, curvature relates to mechanical stress and volume change. We used the simple assumption that for geometrically similar films, the as-measured substrate curvature and volume changes of the active particles correlate linearly. The active material loading of the electrodes was 5 mg cm^{-2} for the cubic phase and 4.5 mg cm^{-2} for the monoclinic phase of HEPBA. The electrode area investigated was about 40 mm^2 in the potential range between 1.5 and 4.5 V vs Na^+/Na at a specific current of 10 mA g^{-1}. 1 M $NaClO_4$ in EC:PC:DMC, 1:1:1 by vol. with 5 vol % FEC was used as electrolyte. Two different cells were investigated in a three-electrode configuration using the substrate curvature setup.

***In Situ* Gas Analysis.** Differential electrochemical mass spectrometry (DEMS) was carried out to investigate the gas

evolution of Cub- and Mono-HEPBA. Cells were assembled using a 30 mm diameter cathode (4.0−4.5 mg cm^{-2} active material loading) with a 4 mm hole in the center, a 40 mm GF/D glass microfiber separator, a 32 mm Na-metal anode, and 700 μL electrolyte (1 M $NaClO_4$ in EC:PC:DMC, 1:1:1 by vol. with 5 vol % FEC) in a customized housing. A 2.5 mL min^{-1} He carrier gas (purity 6.0) flow through this housing was established, and the extracted gas mixture was analyzed by a mass spectrometer (Omni Star GSD320, Pfeiffer Vacuum GmbH) after passing through a −8 °C cold trap to condense electrolyte components, while the cell was cycled between 1.5 and 4.5 V vs Na^+/Na at a specific current of 10 mA g^{-1}. Calibration curves for H_2 and CO_2 are shown in Figure S12 (more details can be found in the literature).[60,61]

AUTHOR INFORMATION

Corresponding Authors

Torsten Brezesinski − *Institute of Nanotechnology (INT), Karlsruhe Institute of Technology (KIT), Karlsruhe 76131, Germany;* orcid.org/0000-0002-4336-263X; Email: torsten.brezesinski@kit.edu

Ben Breitung − *Institute of Nanotechnology (INT), Karlsruhe Institute of Technology (KIT), Karlsruhe 76131, Germany;* orcid.org/0000-0002-1304-3398; Email: ben.breitung@kit.edu

Yanjiao Ma − *School of Energy and Mechanical Engineering, Nanjing Normal University, Nanjing 210023, China;* orcid.org/0000-0002-4125-2867; Email: yanjiao.ma@njnu.edu.cn

Authors

Yueyue He − *Institute of Nanotechnology (INT), Karlsruhe Institute of Technology (KIT), Karlsruhe 76131, Germany*

Sören L. Dreyer − *Institute of Nanotechnology (INT), Karlsruhe Institute of Technology (KIT), Karlsruhe 76131, Germany;* orcid.org/0000-0001-8867-4787

Tolga Akçay − *Institute for Applied Materials (IAM), Karlsruhe Institute of Technology (KIT), Karlsruhe 76131, Germany;* orcid.org/0000-0002-1460-9541

Thomas Diemant − *Helmholtz Institute Ulm (HIU) Electrochemical Energy Storage, Ulm 89081, Germany*

Reiner Mönig − *Institute for Applied Materials (IAM), Karlsruhe Institute of Technology (KIT), Karlsruhe 76131, Germany;* orcid.org/0000-0003-1048-9973

Yuan Ma − *Institute of Nanotechnology (INT), Karlsruhe Institute of Technology (KIT), Karlsruhe 76131, Germany; Confucius Energy Storage Lab, Key Laboratory of Energy Thermal Conversion and Control of Ministry of Education, School of Energy and Environment, Southeast University, Nanjing 211189, China*

Yushu Tang − *Institute of Nanotechnology (INT), Karlsruhe Institute of Technology (KIT), Karlsruhe 76131, Germany*

Huifeng Wang − *Université Paris Cité, CNRS, ITODYS (UMR 7086), Paris 75013, France*

Jing Lin − *Institute of Nanotechnology (INT), Karlsruhe Institute of Technology (KIT), Karlsruhe 76131, Germany*

Simon Schweidler − *Institute of Nanotechnology (INT), Karlsruhe Institute of Technology (KIT), Karlsruhe 76131, Germany;* orcid.org/0000-0003-4675-1072

Maximilian Fichtner − *Helmholtz Institute Ulm (HIU) Electrochemical Energy Storage, Ulm 89081, Germany*

Horst Hahn − *Institute of Nanotechnology (INT), Karlsruhe Institute of Technology (KIT), Karlsruhe 76131, Germany; School of Sustainable Chemical, Biological and Materials Engineering, The University of Oklahoma, Norman, OK 73019, USA*

Author Contributions

Y.H. and Y.-J.M. conceived the idea, designed the experiments, conducted most of the characterizations, analyzed the results, and drafted the manuscript. Y.-J.M. and B.B. supervised the work. T.A. and R.M. contributed to the *operando* stress measurements. S.D. and T.B. performed and analyzed the DEMS experiments. J.L. assisted in the DSC measurements. S.S. assisted in the Rietveld refinement analyses. T.D. and M.F. contributed to the XPS analyses. H.W. assisted in the analysis of *operando* EIS data. Y.T. assisted in the TEM measurements. Y.M. assisted in the SEM imaging. Y.-J.M., T.B., and B.B. provided the main comments on the manuscript. H.H. provided some of the research funding. All authors commented on the manuscript.

Notes

The authors declare no competing financial interest.

ACKNOWLEDGMENTS

Y.H. and H.W. acknowledge financial support from the China Scholarship Council (CSC). J.L. acknowledges the Fonds der Chemischen Industrie (FCI) for financial support. The authors further acknowledge the support from the Karlsruhe Nano Micro Facility (KNMFi, www.knmf.kit.edu.), a Helmholtz research infrastructure at Karlsruhe Institute of Technology (KIT, www.kit.edu). This work contributes to the research performed at CELEST (Center for Electrochemical Energy Storage Ulm-Karlsruhe) and was partly funded by the German Research Foundation (DFG) under project ID 390874152 (POLiS Cluster of Excellence).

REFERENCES

(1) Larcher, D.; Tarascon, J.-M. Towards Greener and More Sustainable Batteries for Electrical Energy Storage. *Nat. Chem.* **2015**, *7*, 19−29.

(2) Gao, M. C.; Miracle, D. B.; Maurice, D.; Yan, X.; Zhang, Y.; Hawk, J. A. High-Entropy Functional Materials. *J. Mater. Res.* **2018**, *33*, 3138−3155.

(3) Shi, X.; Zou, J.; Chen, Z. Advanced Thermoelectric Design: From Materials and Structures to Devices. *Chem. Rev.* **2020**, *120*, 7399−7515.

(4) Yao, Y.; Dong, Q.; Brozena, A.; Luo, J.; Miao, J.; Chi, M.; Wang, C.; Kevrekidis, I. G.; Ren, Z. J.; Greeley, J.; et al. High-Entropy Nanoparticles: Synthesis-Structure-Property Relationships and Data-Driven Discovery. *Science* **2022**, *376* (6589), No. eabn3103.

(5) Xu, W.; Chen, H.; Jie, K.; Yang, Z.; Li, T.; Dai, S. Entropy-Driven Mechanochemical Synthesis of Polymetallic Zeolitic Imidazolate Frameworks for CO_2 Fixation. *Angew. Chem., Int. Ed.* **2019**, *58*, 5018−5022.

(6) Batchelor, T. A. A.; Pedersen, J. K.; Winther, S. H.; Castelli, I. E.; Jacobsen, K. W.; Rossmeisl, J. High-Entropy Alloys as a Discovery Platform for Electrocatalysis. *Joule* **2019**, *3*, 834−845.
(7) Sarkar, A.; Velasco, L.; Wang, D.; Wang, Q.; Talasila, G.; de Biasi, L.; Kübel, C.; Brezesinski, T.; Bhattacharya, S. S.; Hahn, H.; et al. High Entropy Oxides for Reversible Energy Storage. *Nat. Commun.* **2018**, *9*, 3400.
(8) Ma, Y.; Brezesinski, T.; Breitung, B.; Ma, Y. High-Entropy Hexacyanoferrates as Robust Cathode Active Materials for Sodium Storage. *Matter* **2023**, *6*, 313−315.
(9) Lin, L.; Wang, K.; Sarkar, A.; Njel, C.; Karkera, G.; Wang, Q.; Azmi, R.; Fichtner, M.; Hahn, H.; Schweidler, S.; et al. High-Entropy Sulfides as Electrode Materials for Li-Ion Batteries. *Adv. Energy Mater.* **2022**, *12*, 2103090.
(10) Wang, Q.; Sarkar, A.; Wang, D.; Velasco, L.; Azmi, R.; Bhattacharya, S. S.; Bergfeldt, T.; Düvel, A.; Heitjans, P.; Brezesinski, T.; Hahn, H.; Breitung, B. Multi-Anionic and -Cationic Compounds: New High Entropy Materials for Advanced Li-Ion Batteries. *Energy Environ. Sci.* **2019**, *12*, 2433−2442.
(11) Amiri, A.; Shahbazian-Yassar, R. Recent Progress of High-Entropy Materials for Energy Storage and Conversion. *J. Mater. Chem. A* **2021**, *9*, 782−823.
(12) Zhao, C.; Ding, F.; Lu, Y.; Chen, L.; Hu, Y. High-Entropy Layered Oxide Cathodes for Sodium-Ion Batteries. *Angew. Chem., Int. Ed.* **2020**, *59*, 264−269.
(13) Gao, H.; Li, J.; Zhang, F.; Li, C.; Xiao, J.; Nie, X.; Zhang, G.; Xiao, Y.; Zhang, D.; Guo, X.; et al. Revealing the Potential and Challenges of High-Entropy Layered Cathodes for Sodium-Based Energy Storage. *Adv. Energy Mater.* **2024**, *14*, 2304529.
(14) Ma, Y.; Ma, Y.; Wang, Q.; Schweidler, S.; Botros, M.; Fu, T.; Hahn, H.; Brezesinski, T.; Breitung, B. High-Entropy Energy Materials: Challenges and New Opportunities. *Energy Environ. Sci.* **2021**, *14*, 2883−2905.
(15) Ye, Y. F.; Wang, Q.; Lu, J.; Liu, C. T.; Yang, Y. High-Entropy Alloy: Challenges and Prospects. *Mater. Today* **2016**, *19*, 349−362.
(16) George, E. P.; Raabe, D.; Ritchie, R. O. High-Entropy Alloys. *Nat. Rev. Mater.* **2019**, *4*, 515−534.
(17) Wang, X.; Guo, W.; Fu, Y. High-Entropy Alloys: Emerging Materials for Advanced Functional Applications. *J. Mater. Chem. A* **2021**, *9*, 663−701.
(18) Oses, C.; Toher, C.; Curtarolo, S. High-Entropy Ceramics. *Nat. Rev. Mater.* **2020**, *5*, 295−309.
(19) Gild, J.; Zhang, Y.; Harrington, T.; Jiang, S.; Hu, T.; Quinn, M. C.; Mellor, W. M.; Zhou, N.; Vecchio, K.; Luo, J. High-Entropy Metal Diborides: A New Class of High-Entropy Materials and a New Type of Ultrahigh Temperature Ceramics. *Sci. Rep.* **2016**, *6*, 37946.
(20) Yan, X.; Constantin, L.; Lu, Y.; Silvain, J.; Nastasi, M.; Cui, B. $(Hf_{0.2}Zr_{0.2}Ta_{0.2}Nb_{0.2}Ti_{0.2})C$ High-entropy Ceramics with Low Thermal Conductivity. *J. Am. Ceram. Soc.* **2018**, *101*, 4486−4491.
(21) Rost, C. M.; Sachet, E.; Borman, T.; Moballegh, A.; Dickey, E. C.; Hou, D.; Jones, J. L.; Curtarolo, S.; Maria, J.-P. Entropy-Stabilized Oxides. *Nat. Commun.* **2015**, *6*, 8485.
(22) Zhao, C.; Ding, F.; Lu, Y.; Chen, L.; Hu, Y. S. High-Entropy Layered Oxide Cathodes for Sodium-Ion Batteries. *Angew. Chem., Int. Ed.* **2020**, *59*, 264−269.
(23) Sarkar, A.; Wang, Q.; Schiele, A.; Chellali, M. R.; Bhattacharya, S. S.; Wang, D.; Brezesinski, T.; Hahn, H.; Velasco, L.; Breitung, B. High-Entropy Oxides: Fundamental Aspects and Electrochemical Properties. *Adv. Mater.* **2019**, *31*, 1806236.
(24) Lun, Z.; Ouyang, B.; Kwon, D.-H.; Ha, Y.; Foley, E. E.; Huang, T.-Y.; Cai, Z.; Kim, H.; Balasubramanian, M.; Sun, Y.; Huang, J.; Tian, Y.; Kim, H.; McCloskey, B. D.; Yang, W.; Clément, R. J.; Ji, H.; Ceder, G. Cation-Disordered Rocksalt-Type High-Entropy Cathodes for Li-Ion Batteries. *Nat. Mater.* **2021**, *20*, 214−221.
(25) Sarker, P.; Harrington, T.; Toher, C.; Oses, C.; Samiee, M.; Maria, J.-P.; Brenner, D. W.; Vecchio, K. S.; Curtarolo, S. High-Entropy High-Hardness Metal Carbides Discovered by Entropy Descriptors. *Nat. Commun.* **2018**, *9*, 4980.
(26) Castle, E.; Csanádi, T.; Grasso, S.; Dusza, J.; Reece, M. Processing and Properties of High-Entropy Ultra-High Temperature Carbides. *Sci. Rep.* **2018**, *8*, 8609.
(27) Jin, T.; Sang, X.; Unocic, R. R.; Kinch, R. T.; Liu, X.; Hu, J.; Liu, H.; Dai, S. Mechanochemical-Assisted Synthesis of High-Entropy Metal Nitride via a Soft Urea Strategy. *Adv. Mater.* **2018**, *30*, 1707512.
(28) Qin, Y.; Liu, J.-X.; Li, F.; Wei, X.; Wu, H.; Zhang, G.-J. A High Entropy Silicide by Reactive Spark Plasma Sintering. *J. Adv. Ceram.* **2019**, *8*, 148−152.
(29) Zhao, X.; Xue, Z.; Chen, W.; Wang, Y.; Mu, T. Eutectic Synthesis of High-Entropy Metal Phosphides for Electrocatalytic Water Splitting. *ChemSuschem* **2020**, *13*, 2038−2042.
(30) Ma, Y.; Ma, Y.; Dreyer, S. L.; Wang, Q.; Wang, K.; Goonetilleke, D.; Omar, A.; Mikhailova, D.; Hahn, H.; Breitung, B.; et al. High-Entropy Metal−Organic Frameworks for Highly Reversible Sodium Storage. *Adv. Mater.* **2021**, *33*, 2101342.
(31) Ma, Y.; Hu, Y.; Pramudya, Y.; Diemant, T.; Wang, Q.; Goonetilleke, D.; Tang, Y.; Zhou, B.; Hahn, H.; Wenzel, W.; et al. Resolving the Role of Configurational Entropy in Improving Cycling Performance of Multicomponent Hexacyanoferrate Cathodes for Sodium-Ion Batteries. *Adv. Funct. Mater.* **2022**, *32*, 2202372.
(32) Yi, H.; Qin, R.; Ding, S.; Wang, Y.; Li, S.; Zhao, Q.; Pan, F. Structure and Properties of Prussian Blue Analogues in Energy Storage and Conversion Applications. *Adv. Funct. Mater.* **2021**, *31*, 2006970.
(33) Peng, J.; Zhang, W.; Liu, Q.; Wang, J.; Chou, S.; Liu, H.; Dou, S. Prussian Blue Analogues for Sodium-Ion Batteries: Past, Present, and Future. *Adv. Mater.* **2022**, *34*, 2108384.
(34) Xiao, Y.; Xiao, J.; Zhao, H.; Li, J.; Zhang, G.; Zhang, D.; Guo, X.; Gao, H.; Wang, Y.; Chen, J.; et al. Prussian Blue Analogues for Sodium-Ion Battery Cathodes: A Review of Mechanistic Insights, Current Challenges, and Future Pathways. *Small* **2024**, 2401957.
(35) Tang, Y.; Li, W.; Feng, P.; Zhou, M.; Wang, K.; Wang, Y.; Zaghib, K.; Jiang, K. High-Performance Manganese Hexacyanoferrate with Cubic Structure as Superior Cathode Material for Sodium-Ion Batteries. *Adv. Funct. Mater.* **2020**, *30*, 1908754.
(36) Peng, J.; Zhang, B.; Hua, W.; Liang, Y.; Zhang, W.; Du, Y.; Peleckis, G.; Indris, S.; Gu, Q.; Cheng, Z.; et al. A Disordered Rubik's Cube-Inspired Framework for Sodium-Ion Batteries with Ultralong Cycle Lifespan. *Angew. Chem., Int. Ed.* **2023**, *62*, No. e202215865.
(37) He, Y.; Dreyer, S. L.; Ting, Y.-Y.; Ma, Y.; Hu, Y.; Goonetilleke, D.; Tang, Y.; Diemant, T.; Zhou, B.; Kowalski, P. M.; et al. Entropy-Mediated Stable Structural Evolution of Prussian White Cathodes for Long-Life Na-Ion Batteries. *Angew. Chem., Int. Ed.* **2024**, *136*, No. e202315371.
(38) Shang, Y.; Li, X.; Song, J.; Huang, S.; Yang, Z.; Xu, Z. J.; Yang, H. Y. Unconventional Mn Vacancies in Mn−Fe Prussian Blue Analogs: Suppressing Jahn-Teller Distortion for Ultrastable Sodium Storage. *Chem.* **2020**, *6*, 1804−1818.
(39) Pramudita, J. C.; Schmid, S.; Godfrey, T.; Whittle, T.; Alam, M.; Hanley, T.; Brand, H. E. A.; Sharma, N. Sodium Uptake in Cell Construction and Subsequent in Operando Electrode Behaviour of Prussian Blue Analogues, $Fe[Fe(CN)_6]_{1-x} \cdot y\ H_2O$ and $FeCo(CN)_6$. *Phys. Chem. Chem. Phys.* **2014**, *16*, 24178−24187.
(40) Oliver-Tolentino, M.; González, M.; Osiry, H.; Ramos-Sánchez, G.; González, I. Electronic density distribution of Mn−N bonds by a tuning effect through partial replacement of Mn by Co or Ni in a sodium-rich hexacyanoferrate and its influence on the stability as a cathode for Na-ion batteries. *Dalton Trans.* **2018**, *47*, 16492−16501.
(41) Xu, Y.; Wan, J.; Huang, L.; Ou, M.; Fan, C.; Wei, P.; Peng, J.; Liu, Y.; Qiu, Y.; Sun, X.; et al. Structure Distortion Induced Monoclinic Nickel Hexacyanoferrate as High-Performance Cathode for Na-Ion Batteries. *Adv. Energy Mater.* **2019**, *9*, 1803158.
(42) Wang, L.; Lu, Y.; Liu, J.; Xu, M.; Cheng, J.; Zhang, D.; Goodenough, J. B. A Superior Low-Cost Cathode for a Na-Ion Battery. *Angew. Chem., Int. Ed.* **2013**, *52*, 1964−1967.
(43) Murty, B. S.; Yeh, J.-W.; Srikanth, R.; Bhattacharjee, P. P. *High-Entropy Alloys*; Elsevier, 2019.

(44) Huang, Y.; Xie, M.; Zhang, J.; Wang, Z.; Jiang, Y.; Xiao, G.; Li, S.; Li, L.; Wu, F.; Chen, R. A Novel Border-Rich Prussian Blue Synthetized by Inhibitor Control as Cathode for Sodium Ion Batteries. *Nano Energy* **2017**, *39*, 273−283.
(45) Sarhid, I.; Lampre, I.; Dragoe, D.; Beaunier, P.; Palpant, B.; Remita, H. Hexacyano Ferrate (III) Reduction by Electron Transfer Induced by Plasmonic Catalysis on Gold Nanoparticles. *Materials* **2019**, *12*, 3012.
(46) Liu, Y.; He, D.; Han, R.; Wei, G.; Qiao, Y. Nanostructured Potassium and Sodium Ion Incorporated Prussian Blue Frameworks as Cathode Materials for Sodium-Ion Batteries. *Chem. Commun.* **2017**, *53*, 5569−5572.
(47) Biesinger, M. C.; Payne, B. P.; Grosvenor, A. P.; Lau, L. W. M.; Gerson, A. R.; Smart, R. S. C. Resolving Surface Chemical States in XPS Analysis of First Row Transition Metals, Oxides and Hydroxides: Cr, Mn, Fe, Co and Ni. *Appl. Surf. Sci.* **2011**, *257*, 2717−2730.
(48) Zhang, X.; Xia, M.; Liu, T.; Peng, N.; Yu, H.; Zheng, R.; Zhang, L.; Shui, M.; Shu, J. Copper Hexacyanoferrate as Ultra-High Rate Host for Aqueous Ammonium Ion Storage. *Chem. Eng. J.* **2021**, *421*, 127767.
(49) Peng, J.; Wang, J.; Yi, H.; Hu, W.; Yu, Y.; Yin, J.; Shen, Y.; Liu, Y.; Luo, J.; Xu, Y.; et al. A Dual-Insertion Type Sodium-Ion Full Cell Based on High-Quality Ternary-Metal Prussian Blue Analogs. *Adv. Energy Mater.* **2018**, *8*, 1702856.
(50) Wang, W.; Gang, Y.; Peng, J.; Hu, Z.; Yan, Z.; Lai, W.; Zhu, Y.; Appadoo, D.; Ye, M.; Cao, Y.; et al. Effect of Eliminating Water in Prussian Blue Cathode for Sodium-Ion Batteries. *Adv. Funct. Mater.* **2022**, *32*, 2111727.
(51) Yin, J.; Shen, Y.; Li, C.; Fan, C.; Sun, S.; Liu, Y.; Peng, J.; Qing, L.; Han, J. In Situ Self-Assembly of Core − Shell Multimetal Prussian Blue Analogues for High-Performance Sodium-Ion Batteries. *ChemSuschem* **2019**, *12*, 4786−4790.
(52) Fu, F.; Liu, X.; Fu, X.; Chen, H.; Huang, L.; Fan, J.; Le, J.; Wang, Q.; Yang, W.; Ren, Y.; et al. Entropy and Crystal-Facet Modulation of P2-Type Layered Cathodes for Long-Lasting Sodium-Based Batteries. *Nat. Commun.* **2022**, *13*, 2826.
(53) Huang, X.; Yang, C.; You, Y. Polycrystalline Prussian White Aggregates as a High-Rate and Long-Life Cathode for High-Temperature Sodium-Ion Batteries. *ACS Appl. Energy Mater.* **2022**, *5*, 8123−8131.
(54) Liu, X.-H.; Peng, J.; Lai, W.-H.; Gao, Y.; Zhang, H.; Li, L.; Qiao, Y.; Chou, S.-L. Advanced Characterization Techniques Paving the Way for Commercialization of Low-Cost Prussian Blue Analog Cathodes. *Adv. Funct. Mater.* **2022**, *32*, 2108616.
(55) Janzen, M.; Kramer, D.; Mönig, R. Switching from Lithium to Sodium—an Operando Investigation of an $FePO_4$ Electrode by Mechanical Measurements and Electron Microscopy. *Energy Technol.* **2021**, *9*, 2000867.
(56) Yue, Y.; Li, N.; Li, L.; Foley, E. E.; Fu, Y.; Battaglia, V. S.; Clément, R. J.; Wang, C.; Tong, W. Redox Behaviors in a Li-Excess Cation-Disordered Mn−Nb−O−F Rocksalt Cathode. *Chem. Mater.* **2020**, *32*, 4490−4498.
(57) Li, S.; Chen, H.; Zhang, Q.; Deng, H.; Chen, S.; Shen, X.; Yuan, Y.; Ding, Y.; Cheng, Y.; Sun, H.; Zhu, J.; Lu, B. Enhanced Potassium-Ion Storage Performance of Bimetallic-Sulfide Based on Regulatory Reaction Mechanism. *Chem. Eng. J.* **2023**, *466*, 143342.
(58) Tian, R.; Wang, Z.; Liao, J.; Zhang, H.; Song, D.; Zhu, L.; Zhang, L. High-Voltage Stability of Small-Size Single Crystal Ni-Rich Layered Cathode for Sulfide-Based All-Solid-State Lithium Battery at 4.5 V. *Adv. Energy Mater.* **2023**, *13*, 2300850.
(59) Liang, J.; Li, Z.; Cheng, J.; Qin, J.; Liu, H.; Wang, D. Self-Templating Construction of Hollow Microspheres Assembled by Nanosheets with Exposed Active Planes for Sodium Ion Storage. *Nano Res.* **2023**, *16*, 4987−4995.
(60) Berkes, B. B.; Jozwiuk, A.; Vračar, M.; Sommer, H.; Brezesinski, T.; Janek, J. Online Continuous Flow Differential Electrochemical Mass Spectrometry with a Realistic Battery Setup for High-Precision, Long-Term Cycling Tests. *Anal. Chem.* **2015**, *87*, 5878−5883.
(61) Berkes, B. B.; Jozwiuk, A.; Sommer, H.; Brezesinski, T.; Janek, J. Simultaneous Acquisition of Differential Electrochemical Mass Spectrometry and Infrared Spectroscopy Data for in Situ Characterization of Gas Evolution Reactions in Lithium-Ion Batteries. *Electrochem. Commun.* **2015**, *60*, 64−69.
(62) Dreyer, S. L.; Maddar, F. M.; Kondrakov, A.; Janek, J.; Hasa, I.; Brezesinski, T. Elucidating Gas Evolution of Prussian White Cathodes for Sodium-ion Battery Application: The Effect of Electrolyte and Moisture. *Batteries Supercaps* **2024**, *7*, No. e202300595.
(63) Rowden, B.; Garcia-Araez, N. A Review of Gas Evolution in Lithium Ion Batteries. *Energy Rep.* **2020**, *6*, 10−18.
(64) Dreyer, S. L.; Kondrakov, A.; Janek, J.; Brezesinski, T. In Situ Analysis of Gas Evolution in Liquid- and Solid-Electrolyte-Based Batteries with Current and Next-Generation Cathode Materials. *J. Mater. Res.* **2022**, *37*, 3146−3168.
(65) Jung, R.; Metzger, M.; Maglia, F.; Stinner, C.; Gasteiger, H. A. Chemical versus Electrochemical Electrolyte Oxidation on NMC111, NMC622, NMC811, LNMO, and Conductive Carbon. *J. Phys. Chem. Lett.* **2017**, *8*, 4820−4825.
(66) Streich, D.; Erk, C.; Guéguen, A.; Müller, P.; Chesneau, F. F.; Berg, E. J. Operando Monitoring of Early Ni-Mediated Surface Reconstruction in Layered Lithiated Ni-Co-Mn Oxides. *J. Phys. Chem. C* **2017**, *121*, 13481−13486.
(67) Yang, Y.; Liu, E.; Yan, X.; Ma, C.; Wen, W.; Liao, X.-Z.; Ma, Z.-F. Influence of Structural Imperfection on Electrochemical Behavior of Prussian Blue Cathode Materials for Sodium Ion Batteries. *J. Electrochem. Soc.* **2016**, *163*, A2117−A2123.
(68) Patnaik, S. G.; Adelhelm, P. Prussian Blue Electrodes for Sodium-Ion Batteries. In *Sodium-Ion Batteries: Materials, Characterization, and Technology*. Titirici, M.-M.; Adelhelm, P.; Hu, Y.-S., Eds.; Wiley, 2022, pp 167187.
(69) Metzger, M.; Strehle, B.; Solchenbach, S.; Gasteiger, H. A. Hydrolysis of Ethylene Carbonate with Water and Hydroxide under Battery Operating Conditions. *J. Electrochem. Soc.* **2016**, *163*, A1219−A1225.
(70) Lundström, R.; Gogoi, N.; Hou, X.; Berg, E. J. Competing Ethylene Carbonate Reactions on Carbon Electrode in Li-Ion Batteries. *J. Electrochem. Soc.* **2023**, *170*, 040516.
(71) Ge, L.; Song, Y.; Niu, P.; Li, B.; Zhou, L.; Feng, W.; Ma, C.; Li, X.; Kong, D.; Yan, Z.; et al. Elaborating the Crystal Water of Prussian Blue for Outstanding Performance of Sodium Ion Batteries. *ACS Nano* **2024**, *18*, 3542−3552.
(72) Schwenke, K. U.; Solchenbach, S.; Demeaux, J.; Lucht, B. L.; Gasteiger, H. A. The Impact of CO_2 Evolved from VC and FEC during Formation of Graphite Anodes in Lithium-Ion Batteries. *J. Electrochem. Soc.* **2019**, *166*, A2035−A2047.
(73) Wang, J.; Dreyer, S. L.; Wang, K.; Ding, Z.; Diemant, T.; Karkera, G.; Ma, Y.; Sarkar, A.; Zhou, B.; Gorbunov, M. V.; Omar, A.; Mikhailova, D.; Presser, V.; Fichtner, M.; Hahn, H.; Brezesinski, T.; Breitung, B.; Wang, Q. P2-Type Layered High-Entropy Oxides as Sodium-Ion Cathode Materials. *Mater. Futures* **2022**, *1*, 035104.
(74) Li, Z.; Dadsetan, M.; Gao, J.; Zhang, S.; Cai, L.; Naseri, A.; Jimenez-Castaneda, M. E.; Filley, T.; Miller, J. T.; Thomson, M. J.; et al. Revealing the Thermal Safety of Prussian Blue Cathode for Safer Nonaqueous Batteries. *Adv. Energy Mater.* **2021**, *11*, 2101764.
(75) Blanchard, W. R.; McCarthy, P. J.; Dylla, H. F.; LaMarche, P. H.; Simpkins, J. E. Long-term Changes in the Sensitivity of Quadrupole Mass Spectrometers. *J. Vac. Sci. Technol. A* **1986**, *4*, 1715−1719.
(76) Batey, J. H. The Physics and Technology of Quadrupole Mass Spectrometers. *Vacuum* **2014**, *101*, 410−415.
(77) Yan, X.; Yang, Y.; Liu, E.; Sun, L.; Wang, H.; Liao, X.-Z.; He, Y.; Ma, Z.-F. Improved Cycling Performance of Prussian Blue Cathode for Sodium Ion Batteries by Controlling Operation Voltage Range. *Electrochim. Acta* **2017**, *225*, 235−242.
(78) Kvamme, B. Kinetics of Hydrate Formation, Dissociation and Reformation. *Chem. Thermodyn. Therm. Anal.* **2021**, *1*, 100004.
(79) Galwey, A. K. Dehydration of Crystalline Hydrates. *Handb. Therm. Anal. Calorim.* **2003**, *2*, 595−656.

(80) Choi, Z.; Kramer, D.; Mönig, R. Correlation of Stress and Structural Evolution in $Li_4Ti_5O_{12}$-Based Electrodes for Lithium Ion Batteries. *J. Power Sources* **2013**, *240*, 245−251.
(81) Stoney, G. G. The Tension of Metallic Films Deposited by Electrolysis. *Proc. R. Soc. A: Math. Phys. Eng. Sci.* **1909**, *82*, 172−175.